The Astrophysical Journal, 1010:145 (24pp), 2026 October 20 https://doi.org/10.3847/1538-4357/aea090
© 2026. The Author(s). Published by the American Astronomical Society.
OPEN ACCESS

The Lazuli Space Observatory: Architecture and Capabilities

Arpita Roy[1], Stuart Feldman[1], Peter Klupar[2], John DiPalma[2], Saul Perlmutter[3,4], Ewan S. Douglas[5], Greg Aldering[4], Gabor Furesz[1], Patrick Ingraham[5], Gudmundur Stefansson[1,6], Douglas Kelly[5], Fan Yang Yang[2], Thomas Wevers[1], Nicole Arulanantham[1], James Lasker[1], Mickael Rigault[7], Everett Schlawin[1], Sander R. Zandbergen[2], S. Pete Worden[2], Ramya Anche[5], Heejoo Choi[5], Ian J. M. Crossfield[8], Kevin Derby[5], Jerry Edelstein[9], Mike Eiklenborg[5], Suvi Gezari[10], Paul Giuliano[2], Justin Hom[5], Taylor J. Hoyt[3], Hyukmo Kang[5], Daewook Kim[5], Keerthi Kunnumkai[11], Leander Lacroix[7], Jared R. Males[5], Thomas J. Maccarone[12], Kian Milani[5], Timothy N Miller[9], Kelsey Lynn Miller[5], Pierre Nicolas[5], Antonella Palmese[11], Jason Pero[8], Laurent Pueyo[13], Stephanie Rinaldi[5], David J. Sand[5], Christian Schneider[14], Sanchit Sabhlok[5], Arfon Smith[1], Irina I. Stefan[5], Saraswathi Kalyani Subramanian[5], Kyle Van Gorkom[5], Andre F. Wong[5], Jaegun Yoo[5], and Md Abdullah Al Zaman[8]
[1] Astrophysics & Space Center, Schmidt Sciences, New York, NY 10011, USA
[2] Project Pearl, Schmidt Sciences, New York, NY 10011, USA
[3] University of California, Berkeley, CA 94720, USA
[4] Lawrence Berkeley National Laboratory, Berkeley, CA 94720, USA
[5] Department of Astronomy and Steward Observatory, University of Arizona, Tucson, AZ 85721, USA
[6] Anton Pannekoek Institute for Astronomy, University of Amsterdam, Science Park 904, 1098 XH Amsterdam, The Netherlands
[7] Universite Claude Bernard Lyon 1, CNRS, IP2I Lyon / IN2P3, IMR 5822, F-69622 Villeurbanne, France
[8] Department of Physics and Astronomy, University of Kansas, Lawrence, KS 66045, USA
[9] Space Sciences Laboratory, University of California, Berkeley, Berkeley, CA 94720, USA
[10] Department of Astronomy, University of Maryland, College Park, MD 20742, USA
[11] Department of Physics, Carnegie Mellon University, Pittsburgh, PA 15213, USA
[12] Department of Physics & Astronomy, Texas Tech University, Box 41051, Lubbock, TX 79409-1051, USA
[13] Space Telescope Science Institute, 3700 San Martin Dr, Baltimore, MD 21218, USA
[14] ITAP, Kiel University, Leibnizstrasse 15, 24118 Kiel, Germany
Received 2026 January 6; revised 2026 August 25; accepted 2026 August 28; published 2026 October 13

Abstract

The Lazuli Space Observatory is a 3 m aperture astronomical facility designed for rapid-response observations and precision astrophysics across visible to near-IR wavelengths (400–1700 nm bandpass). An off-axis, freeform telescope delivers diffraction-limited image quality (Strehl >0.8 at 633 nm) to three instruments across a wide, flat focal plane. The three instruments provide complementary capabilities; the Wide-field Context Camera (WCC) delivers multiband imaging over a $35' \times 12'$ footprint with high-cadence photometry; the Integral-field Spectrograph (IFS) provides continuous 400–1700 nm spectroscopy at $R \sim$ 100–500 for stable spectrophotometry; and the ExtraSolar Coronagraph (ESC) enables high-contrast imaging expected to reach raw contrasts of 10^{-8} and postprocessed contrasts approaching 10^{-9}. Operating from a 3:1 lunar-resonant orbit, Lazuli will respond to targets of opportunity in under four hours—a programmatic requirement designed to enable routine temporal responsiveness that is unprecedented for a space telescope of this size. Lazuli's technical capabilities are shaped around three broad science areas: (1) time-domain and multimessenger astronomy, (2) stars and planets, and (3) cosmology. These capabilities enable a potent mix of science spanning gravitational-wave counterpart characterization, fast-evolving transients, Type Ia supernova cosmology, high-contrast exoplanet imaging, and spectroscopy of exoplanet atmospheres. While these areas guide the observatory design, Lazuli is conceived as a general-purpose facility with open time for the global community. We describe the observatory architecture and capabilities in the preliminary design phase, with science operations anticipated following a rapid development cycle from concept to launch; quoted performance specifications reflect current design requirements and modeling predictions, pending on-orbit verification.

Unified Astronomy Thesaurus concepts: Space telescopes (1547); Astronomical instrumentation (799); Coronagraphic imaging (313); Spectroscopy (1558); Time domain astronomy (2109); Gravitational wave sources (677); Exoplanet astronomy (486); Cosmology (343)

1. A Philanthropic Approach to Astrophysics

Over the past decade, the landscape of space-based astronomy has shifted toward greater emphasis on rapid development, focused instrument suites, and responsiveness to time-critical science. The Lazuli Space Observatory is designed to embody this shift, with two primary goals: to deploy and operate a world-class astronomical observatory in space, and to do so on a substantially accelerated and lower-cost development timeline relative to traditional approaches. The project is underway, with secured funding and a defined budget, as well as detailed plans for the instruments, spacecraft, and development schedule.

The Lazuli Space Observatory is part of a larger program—the Eric and Wendy Schmidt Observatory System—which will include at least three ground-based observatories as well as

Original content from this work may be used under the terms of the Creative Commons Attribution 4.0 licence. Any further distribution of this work must maintain attribution to the author(s) and the title of the work, journal citation and DOI.

one or more space-based observatories. Each ground-based telescope adopts a similarly risk-tolerant approach, leveraging large numbers of smaller components and modern computing to achieve scalable performance. All of these facilities are pure research instruments intended to enable deeper understanding of the Universe. They are designed to support global community use through rapid, open dissemination of data.

The Lazuli Space Observatory concept presented here draws from an initial mission concept and a subsequent study led through the Space Sciences Laboratory at University of California, Berkeley, which articulated a high-risk, high-speed paradigm for large-aperture space astronomy on large-capacity launch vehicles (LVs), exemplified by a first mission combining an integral-field spectrograph (IFS) and an imager to address timely dark energy science, as well as the nimble follow-up of gravitational-wave events, exoplanet transits, and other transients. The feasibility study included a coronagraph that was developed by E. S. Douglas et al. (2023), with active wave front control based on a laboratory-tested design. We initially explored various designs, prototypes, and evaluations for this notional 6.5 m mission focused on much more specific science objectives. That approach ultimately proved infeasible within our desired time, risk, and financial constraints.

In late 2024, the project pivoted to the observatory architecture described here, which was approved for construction in mid-2025. The Lazuli Space Observatory employs a 3 m primary mirror (PM) and a broader, more detailed science program designed to take full advantage of the coronagraph, camera, and spectrograph.

The Lazuli Space Observatory is funded privately, a first for a space mission of this scale. Philanthropic funding can help fill the gap between relatively small, rapid missions and very ambitious but expensive and decades-long flagship projects. Engineering for the Lazuli Space Observatory is based on existing cutting-edge technologies, while project management builds on decades of experience across government, academic, and industrial space programs, incorporating lessons learned from the development and operations of large space telescope facilities, as well as the broader commercial space sector. The instrument suite will enable a wide range of important observing campaigns while remaining deliberately constrained to limit observatory complexity. The Lazuli Space Observatory is designed to be launchable within approximately 3–5 yr of the start of detailed planning. This effort is intended to demonstrate a viable pathway for deploying significant astronomical instrumentation on accelerated timescales.

This paper is the first in a series describing the Lazuli Space Observatory and its scientific capabilities. It begins by outlining the science motivation for Lazuli (Section 2) and the broader development approach it represents, followed by a description of the mission design guidelines that translate those motivations into concrete architectural choices (Section 3). We then present the observatory architecture and design in detail (Section 4), followed by the scientific capabilities enabled by those designs (Section 5). Section 6 describes the mission operations concept, including orbit selection and scheduling strategies optimized for rapid response. Section 7 outlines community access, data policies, software, and engagement frameworks. We conclude in Section 8 with a synthesis of Lazuli's role within the evolving landscape of space-based astrophysics.

2. Science Motivation

Lazuli is designed to move cutting-edge technology into the hands of astronomers faster than traditional mission development timelines, with a goal to accelerate exciting astrophysical discoveries. This approach accepts a higher risk profile in exchange for rapid scientific return, and provides the opportunity to fly promising but lower-heritage technologies that might otherwise await slow derisking timelines. Our science capabilities are chosen to be both transformative for this decade and achievable within a 3–5 yr development timeline from concept to launch. Even though the Lazuli team approached this question from the perspective of rapid development for impactful science, our priorities are well aligned with the recommendations of the Astro2020 Decadal Survey (National Academies of Sciences et al. 2021) and complement existing and planned observatories by performing precursor observations allowing target and technique optimizations for future missions, technology maturation, and follow-up of high-value targets.

2.1. Rapidly Responding to a Transient Universe

The advent of wide-field time-domain surveys has revealed a transient Universe that demands rapid spectroscopic follow-up. Gravitational-wave electromagnetic counterparts fade rapidly, often within hours to days (e.g., GW170817; B. P. Abbott et al. 2017); fast blue optical transients (FBOTs) evolve on hour-to-day timescales (e.g., AT2018cow; S. J. Prentice et al. 2018); and early-time observations of supernovae (SNe) provide critical constraints on progenitor systems and explosion physics (e.g., E. Waxman & B. Katz 2017). Current large space-based facilities, while exquisitely sensitive, respond to targets of opportunity on timescales of days to weeks—often too late to capture the most rapidly evolving phenomena. A notable exception is Swift, which can respond to targets of opportunity (ToOs) on timescales of minutes but has a much smaller aperture. Ground-based telescopes can respond quickly but face fundamental limitations: atmospheric emission and absorption, weather and diurnal interruptions, and seeing-limited resolution. With large sky surveys from the Rubin Observatory (Ž. Ivezić et al. 2019), Nancy Grace Roman Space Telescope (D. Spergel et al. 2015), Argus (N. M. Law et al. 2022), and ULTRASAT (Y. Shvartzvald et al. 2024) imminent, and upgraded gravitational-wave detectors coming online in the late 2020s, the astronomical community will discover transients at unprecedented rates—but lacks a space-based platform to characterize them spectroscopically within hours. Lazuli addresses this gap directly. With a threshold response time <4 hr from trigger receipt to first observation (with a goal of 90 minutes), the observatory is designed to capture transient phenomena during their earliest evolutionary phases—when physical conditions change most rapidly.

2.2. Flying Ambitious Technology to Accelerate Science Readiness

Several of Lazuli's key capabilities rely on technologies with limited space flight heritage but strong technical maturity and high scientific potential. For example, high-contrast imaging of exoplanets from space offers exceptional potential for understanding planetary systems, but the technique requires iteration between laboratory demonstrations and on-

orbit experience to achieve the contrasts needed for detecting true Earth analogs (G. Ruane et al. 2018; N. J. Kasdin et al. 2020; B. Mennesson et al. 2024). Lazuli embraces the opportunity to fly coronagraphic technologies with low space heritage but high science potential for science usage now—accepting higher risk in exchange for expanded astrophysical returns and operational lessons that cannot be learned on the ground (E. S. Douglas et al. 2023). The goal of flying such technology on Lazuli is to produce valuable science in its own right while building the heritage needed for future flagship missions such as the Habitable Worlds Observatory (HWO; National Academies of Sciences et al. 2021). This approach—prototyping technology and proceeding directly to flight rather than waiting for hierarchical derisking—accelerates both scientific return and technical readiness for the missions that will ultimately perform deeper searches for life beyond Earth.

2.3. Sustaining Large-aperture Optical–Near-infrared Capability in Space

Finally, Lazuli addresses a growing need for large-aperture optical–near-IR (NIR) capability in space. The Hubble Space Telescope (HST) has served the astronomical community for over three decades and remains scientifically productive, but as the sole flagship-class space observatory operating at optical and UV wavelengths, it faces intense proposal pressure (Space Telescope Science Institute 2024), and no planned facility provides equivalent or stronger capabilities until the HWO in the early 2040s (National Academies of Sciences et al. 2021). The James Webb Space Telescope (JWST), while transformative in the IR, operates at wavelengths redder than 600 nm (J. P. Gardner et al. 2006), and is already facing the highest proposal pressure of any large observatory (R. Rao 2024). The upcoming Roman Space Telescope, launched in 2026, will image the NIR sky at wavelengths redder than 500 nm and will acquire $R \sim 100$–600 spectroscopy at $\lambda > 750$ nm (D. Spergel et al. 2015; R. Akeson et al. 2019) but is optimized for wide-field survey science rather than rapid-response, targeted spectroscopic follow-up or high-cadence observations. Lazuli instead occupies a complementary observational niche. It is designed to provide rapid-response, diffraction-limited optical and NIR imaging and spectroscopy, with an operations model centered on time-critical observations and instruments that incorporate decades of advances in optical–NIR detector technology, instrument design, and mission operations. These capabilities differ from, rather than replace, HST's strengths. In the spirit of HST's enduring legacy (e.g., N. G. Roman 1974), Lazuli aims to serve a broad range of existing science needs while holding capability for ideas yet to come.

3. Mission Design Guidelines

Lazuli represents an experiment in space observatory development for astrophysics, borrowing from successful "new space" approaches in industry. Rather than following the traditional flagship model—where technology is invented, matured over decades, and flown for science use after comprehensive risk reduction—Lazuli aims to demonstrate a different development curve. Rather than envision and create new technology ab initio, we apply available technology in novel ways—building on the heritage of research and development from major international partnerships and decades of ground-based and space-based astronomy.

The mission design is guided by a set of Level-0 (L0) program objectives that flow from two overarching goals: to demonstrate a different and more rapid approach to large-aperture space observatory development, and to provide a world-class astrophysics facility to the global scientific community. The following principles shape major design decisions for Lazuli:

1. *Schedule as a feature, not a constraint.* Lazuli is designed to launch and operate while the science questions it addresses remain pressing and while synergistic facilities—including Rubin Observatory, the Roman Space Telescope, and gravitational-wave detector networks—are active. A compressed development timeline is not a compromise but a deliberate design choice that maximizes scientific relevance and responsiveness to community needs.
2. *Risk tolerance as a driver of cost discipline.* Lazuli is intentionally positioned in a different region of the cost–risk trade space than traditional flagship missions, enabling accelerated development and near-term scientific return. This posture constrains cost by reducing the need for prolonged technology maturation and exhaustive preflight risk retirement, with risk acceptance bounded through focused requirements, selective use of heritage, and an operations concept designed for on-orbit learning. Unlike some flagship observatories and designs, Lazuli is not designed to be serviceable, keeping cost and complexity down.
3. *Rapid response as a primary design driver.* The capability to observe transient phenomena within hours of discovery is not an enhancement but rather a foundational requirement that shapes spacecraft design, mission operations, and ground system architecture.
4. *Focused instrument suite.* Limiting the number of modes, as well as focusing on core performance verification, mitigates the schedule delays and cost growth that commonly arise when complex instrument suites with competing requirements must achieve simultaneous readiness.
5. *Coordination over competition.* Lazuli is intended to complement and enhance the scientific return of other facilities rather than replicate their capabilities. Data will be released promptly to maximize benefit to the broader community.
6. *General-purpose by intent.* Specific science cases serve as tools to anchor broad capability, but Lazuli is conceived as a general-purpose facility—capable of supporting research well beyond what is described here, including questions that have not yet been formulated—maintaining flexibility for investigations that will emerge over the mission lifetime.

These principles inform the observatory architecture, operations concept, and science capabilities described in the sections that follow. Lazuli's development has been driven by an iterative process; technical capabilities were chosen to enable specific science goals, while the science scope has evolved in response to realistically achievable technical performance—a parallel development approach that reflects

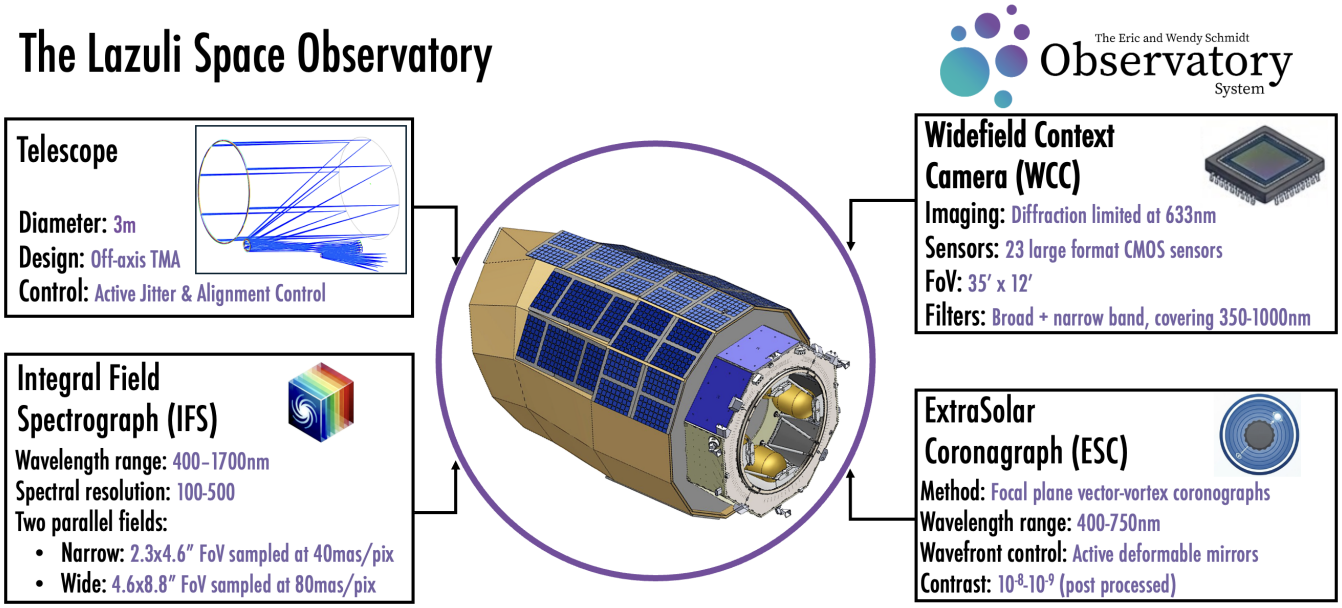

Figure 1. Overview of the 3 m Lazuli Space Observatory and its three instruments: WCC, IFS, and ESC. Main properties and characteristics of the telescope and the instruments are highlighted.

the mission's compressed timeline, a strategy consistent with agile systems engineering best practices.

4. Observatory Architecture and Design Capabilities

4.1. Observatory Overview

The Lazuli Space Observatory will be a dedicated 4000 kg space-based astronomical facility that will operate in a highly elliptical lunar-resonant orbit. The observatory comprises an off-axis three-mirror anastigmat (TMA) telescope with a 3 m PM unobscured by the secondary mirror (SM)—a configuration that delivers diffraction-limited point-spread function (PSF) quality across a wide focal plane (Section 4.3). The observatory has a nominal lifetime requirement of 3 yr and is provisioned with consumables to support a 10 yr extended-mission goal.

Three science instruments provide complementary capabilities spanning imaging, spectroscopy, and high-contrast coronagraphy. The Wide-field Context Camera (WCC; Section 4.4) delivers imaging across 350–1000 nm with broadband and narrowband filters, in-focus and defocused configurations, and high-cadence readout modes. The IFS (Section 4.5) provides continuous spectral coverage from 400–1700 nm at a spectral resolution $R \sim 100$–500. The ExtraSolar Coronagraph (ESC; Section 4.6) employs a vector vortex coronagraph with active wave front control, leveraging the effectively unobscured aperture to enable high-contrast imaging of nearby extrasolar systems. Figure 1 provides an overview of the observatory and its instruments; Table 1 summarizes key parameters.

4.2. Spacecraft Bus

The science payload will be integrated with a flight-proven spacecraft bus that provides propulsion, attitude and orbit control, power, communications, and command and data handling, while maintaining independent thermal management. The bus design leverages heritage avionics and propulsion architectures derived from prior space missions, including lunar-resonant and deep-space platforms, while employing a bespoke structure optimized for high pointing stability. The payload optical bench utilizes low coefficient of thermal expansion (CTE) materials, while body-mounted solar panels eliminate appendage modes that could disturb pointing stability.

Three-axis attitude determination is provided by three star trackers and two inertial reference units based on solid-state Coriolis vibratory gyroscopes. Six reaction wheels in a skewed configuration provide torque authority for slewing, attitude maintenance, and momentum management. At the payload level, residual line-of-sight (LOS) motion is measured using guide-star observations from the WCC and corrected by the telescope Fast Steering Mirror (FSM).

The observatory is designed for compatibility with multiple LVs via a standard 2.6 m interface, with injection to a supersynchronous transfer orbit. The monopropellant hydrazine propulsion system provides $\delta v \sim 450$ m s^{-1}, of which $\sim$250 m s^{-1} is allocated to the transfer to the operational Highly Elliptical Orbit (HEO) via a lunar gravity assist. The remaining propellant is allocated to attitude momentum management, contingency, and margin. The lunar-resonant orbit operates outside Earth's trapped radiation belts, reducing radiation-induced noise and total ionizing dose environment, while providing thermal stability for cryogenic systems (Section 6.1). Continuous access to a commercial ground station network enables high-bandwidth science data downlink and uplink commanding for real-time observation tasking. The system is designed to deliver an average of 70 GB day^{-1} of mission data. LOS stability is achieved through a multitiered strategy. Primary reaction wheel disturbances are minimized at the source through strict unbalance limits and further attenuated by a passive isolation system. The structural design actively avoids placing key modes near wheel harmonics, while operational protocols enforce accelerated pass-throughs to prevent amplification at critical resonances. An FSM is commanded to suppress adverse LOS motion at or below wheel isolator frequency bands. Science data handling

Table 1
Overview of the Lazuli Space Observatory, the Telescope, Instruments, and Key Parameters

Parameter	Value
Telescope:	
Optical layout	Off-axis TMA
PM	3.06 m (effective diameter)
F/# and field of view (FOV)	F/15, $0.^{\circ}5 \times 0.^{\circ}25$
Image quality (target)	Strehl ratio >0.8 at 633 nm (incl. jitter)
WCC:	
Wavelength range	350–1000 nm
Instrument + Telescope throughput	>50% at 600 nm
Science sensors (×15)	**Model and packaging:** Sony IMX 455 **Sensor size:** 9568 × 6380 pixels, 864mm^2 **Plate scale:** 17 mas/pix for each 3.76μm pixel **Read noise:** $<2e^-$ **Dark noise:** 0.0015 e/s/pix (current best estimate at −20C)
Science + Guide sensors (×8)[a]	**Model and packaging:** BAE qCMOS HWK 4123 **Sensor size:** 4096 × 2304 pixels, 200mm^2 **Plate scale:** 21 mas/pix for each 4.6μm pixel **Read noise:** $<0.3e^-$ **Dark noise:** 0.004 e s^{-1} pix^{-1} (current best estimate at −20C)
IFS	
Wavelength range	400–1700 nm
Instrument throughput	Threshold: >40% from 400–1000nm; >50% from 1000–1700 nm
Detector	Teledyne H4RG-10 HgCdTe (1700 nm cutoff)
Spectral resolution[b]	100–500
Observing Fields	**NF:** $2.''3 \times 4.''6$ FOV sampled at 40 mas/pix **WF:** $4.''6 \times 8.''8$ FOV sampled at 80 mas/pix
ESC:	
Wavelength range	**Blue Arm:** 400–540 nm **Red Arm:** 560–750 nm with multiple (>5) filters
Instrument throughput	⩾2% at 630 nm
Wave front control	Active DMs
Inner (IWA) and outer working angles (OWA)	IWA ⩽ $0.''15$ (goal of $0.12''$); OWA ⩾ $0.''4$ (goal of $0.6''$) at 630 nm
(Anticipated) Raw contrast	10^{-8}
(Anticipated) Postprocessed contrast	10^{-9}
Orbit:	
Type	3:1 lunar-resonant orbit
Period	9 days
Perigee and apogee	70,000 km, 285,000 km
Min field coverage	130 days
Field of regard	24,200 deg^2 (2.35π sr.; goal 3.3π sr.)
CVZ	Ecliptic latitude $\lvert\beta\rvert \geqslant 54°$

Notes. Throughputs and detector noise properties are listed as modeled beginning-of-life specifications.
[a] Although during regular operations, one qCMOS sensor is envisioned to be used for active guiding, the qCMOS sensors will also be available for scientific observations, especially to capitalize on their low read noise and sensitivity at redder wavelengths.
[b] Using a prism dispersing element, the spectral resolution reaches a minimum of ∼100 at 1000 nm and rises to ∼500 at the blue, and to ∼200 at the red ends, respectively.

includes an X-band downlink to a network of commercial ground stations. The design supports multiyear mission operations with critical subsystem redundancy.

4.3. Optical Telescope Assembly

Lazuli is designed around an off-axis TMA telescope with an optically monolithic primary mirror (PM) of 3 m diameter. The PM construction follows a novel, proprietary approach, using lightweight, thermally stable, low CTE materials including silicon carbide (SiC). The design traces its heritage to commercially flying telescopes that deliver diffraction-limited image quality in the visible, and also incorporates lessons learned from technologies developed for the JWST optics production. A key enabling factor behind Lazuli is its deep technological heritage drawn from these prior space programs and ground-based telescopes, as well as the use of active in-orbit alignment technology and jitter control. This informs the architectural choices and performance modeling underlying the telescope design, enabling Lazuli not only to meet its optical performance requirements but also to support the mission's demanding development and deployment schedule.

The large, effectively unobscured, (kinematically) passive PM provides a unique opportunity for coronagraphy, while the freeform TMA design enables a large aberration-balanced field of view that provides diffraction-limited PSFs to host multiple instruments. Controlling the telescope's exit pupil on a fourth flat FSM enables jitter compensation which, along with the careful design of the bus and the attitude control system (ACS), is designed to meet tight pointing requirements enabling the observatory's diffraction-limited image quality targets at 633 nm. The telescope structure largely relies on lightweight and low CTE structural materials. The selection of orbit, optical materials, concept of operations, and internal thermal design together ensure that Lazuli achieves both rapid and low-amplitude thermal settling between slews, once the payload and telescope structure have been aligned and stabilized on orbit during commissioning. Figure 2 shows expected model predictions for the as-built in-orbit image quality across the Lazuli focal plane.

4.4. WCC

The WCC is a diffraction-limited (Strehl >0.8 at a reference wavelength of 633 nm) wide-field imager with a $35' \times 12'$ footprint. The focal plane is populated with an array of 23 CMOS sensors (providing a sensor fill factor of ∼0.2, although there is an additional ±15° flexibility in the telescope roll angle around the boresight that provides increased sky coverage), each equipped with a fixed photometric filter (Figure 3). Exact filter positions and arrangements are notional at this stage and subject to further optimization.

The WCC employs two detector types: the Sony IMX 455 CMOS sensor and the BAE HWK 4123 qCMOS sensor. The IMX 455 provides a larger field of view ($2.7' \times 1.8'$ per sensor) and constitutes the majority of the array (15 sensors). The HWK 4123 offers a smaller field of view ($1.'4 \times 0.'8$ per sensor), but achieves subelectron readout noise (RON $<0.3e^-$), improving the limiting magnitude for low signal-to-noise ratio (S/N) (< 10) sources by ∼1.5 mag compared to the IMX 455 (RON $\sim 2e^-$). This low read noise is important to reach >99% guide-star availability in the field of regard and fast closing of the FSM control loop. As such, the WCC is not just a science instrument but also provides core functionality to the observatory through guide-star observations. Each PSF is sufficiently sampled by multiple pixels, and certain sensors are permanently offset in focus to provide service to other instruments (e.g., PSF knowledge for the IFS through phase retrieval wave front sensing) or to enable the highest possible

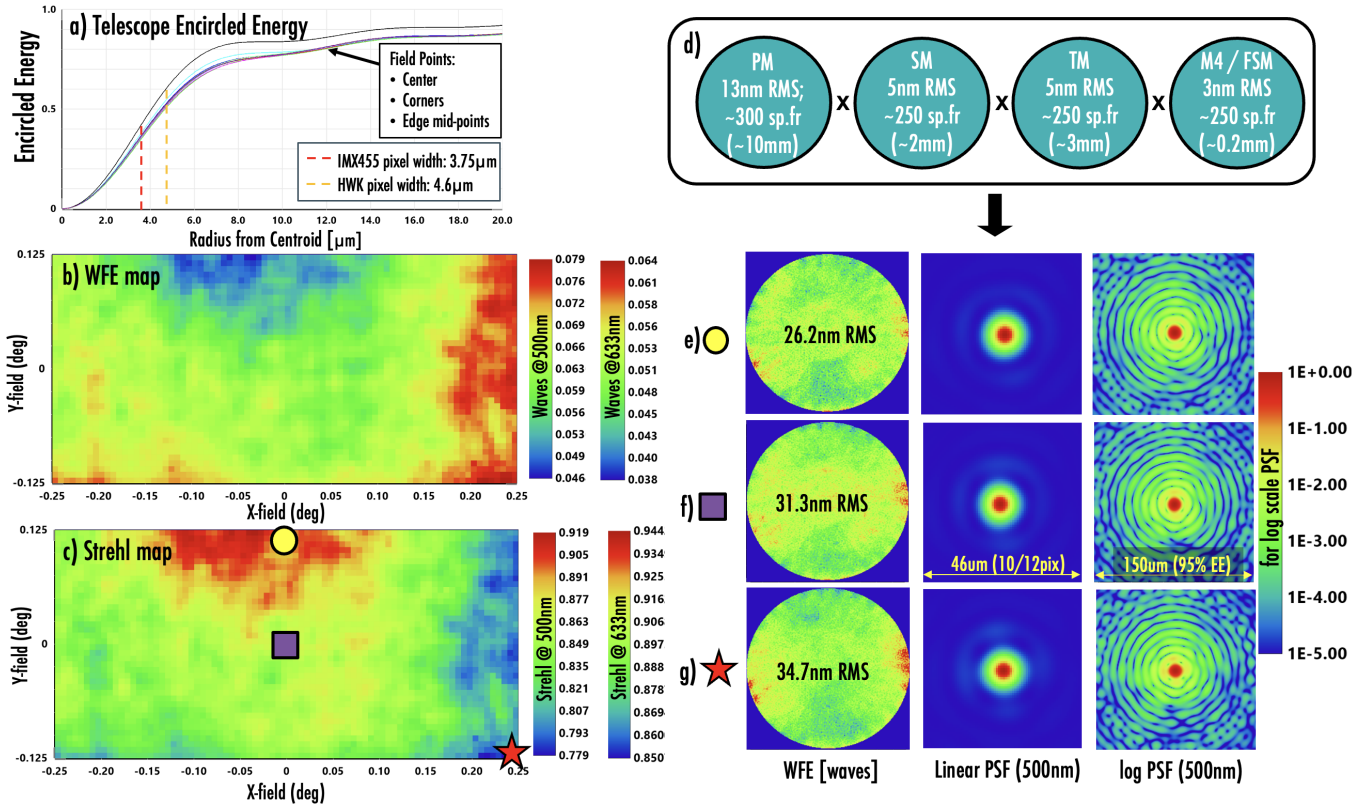

Figure 2. Current model prediction for the as-built in-orbit image quality across the Lazuli focal plane. This accounts for surface figure errors across all four optical elements (PM, SM, TM, and FSM), residual alignment errors, and thermal distortion errors of the PM of the TMA telescope. (a) Encircled energy versus radius at various field points compared to the diffraction limit (black). Dashed vertical lines indicate the pixel size of the WCC sensors (red: Sony IMX 455; orange: HWK 4123). (b) Wave front error map in waves across the telescope focal plane with color bars for 500 and 633 nm. (c) Strehl ratio map of the same area. (d) Surface figure assumptions for the four telescope optical elements—PM, SM, tertiary mirror (TM), and FSM, showing the rms wave front and number of spatial frequencies (sp.fr.). The contribution of each of the four optics is multiplicatively combined to form the wave front map, linear PSF, and log-color bar PSF shown in (e), (f), and (g). The circle, square, and star in c) indicate the field points which are shown in (e), (f), and (g).

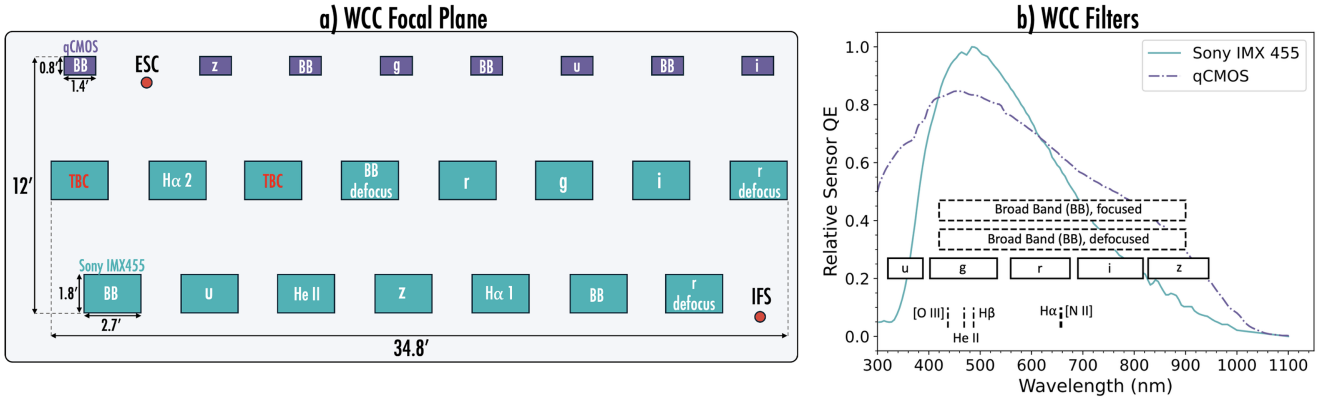

Figure 3. (a) Overview of the WCC focal plane showing the distribution of the sensors on the focal plane. Sony IMX sensors are shown in turquoise, and HWK qCMOS sensors are shown in purple. The entrance apertures to the IFS and ESC instruments are also indicated with the red circles. Filter locations are subject to change pending instrument design optimization. Possibilities for the "TBC" filter locations are discussed in the main text. (b) Overview of the WCC filter suite as a function of wavelength. The nominal quantum efficiency of the Sony IMX 455 and the HWK 4123 qCMOS sensors are shown as solid black and dotted–dashed green lines, respectively.

photometric precision by integrating over pixel-to-pixel and subpixel systematics.

The WCC will cover the visible wavelength range from the blue to the red sensitivity cutoffs of the silicon sensors, 350–1000 nm (Figure 3 right panel). The filter set will include both broad- and narrowband filters, including Sloan-like *u*, *g*, *r*, *i*, *z* bands, along with a broadband filter to enable high-precision exoplanet transit science in integrated light. One of these filters will be for an in-focus sensor, while another will be for an out-of-focus sensor. Narrowband filters will notionally include two Hα filters of different widths (nominally 2 nm and 6 nm in width, indicated as Hα-1 and Hα-2 in Figure 3), along with a He II filter. Additional possible narrow band filters are being considered for the two remaining

slots indicated as 'to be confirmed (TBC)' in Figure 3, including Hβ, [O III], and [N II].

In addition to full-frame imaging, all detectors are capable of operating in region-of-interest windowed modes, nominally with frame rates up to at least 200 Hz. The combination of wide-field, low-read-noise detectors with a diffraction-limited 3 m aperture optical system will serve a very broad range of science interests, including spatially resolved studies of extended sources and in crowded fields, high-precision photometry, high temporal resolution ($\sim$5 ms) science, and very faint source imaging.

The TMA design enables simple accommodation and low-risk operation of the WCC, with no moving parts required for the photometric sensors in a focal-plane layout intentionally configured to balance science, guiding, and wave-front-sensing requirements (see Figure 3). This design choice, however, requires multiband observations of a given source to be obtained via telescope offsets that sequentially place the target on the desired sensors. Nevertheless, multiple sensors can be operated simultaneously to improve the efficiency of large mosaicking observations or to enable parallel investigations when target placement and guide-star availability permit. Such parallel observations can also be carried out when the WCC is not the primary instrument, enabling ancillary science programs—for example, the construction of deep-field mosaics as a by-product of repeated visits to the same region or deep integrations obtained concurrently with IFS observations.

Lazuli's rapid-response capability will make the WCC a transient workhorse, but dynamic scheduling is a more necessary capability for that science than pure photometric precision. The WCC noise floor will have the largest impact on transiting exoplanet observations, and we discuss the expected performance of the chosen architecture in this context. As an example of the expected on-sky performance of the WCC, Figure 4 shows the expected photometric precision (and S/N) of the WCC Sloan-like *r* filter as a function of stellar magnitude for one of the in-focus *r*-band sensors. The precision estimates include contributions from photon, read, dark, and sky-background noise. Observations of the brightest stars will be systematics-limited—especially at long binning timescales—setting a systematic photometric precision noise floor due to contributions from a combination of imperfect detectors, calibrations, varying background light, and astrophysical sources of noise. In Figure 4, we assume a noise floor of 20 ppm, comparable to the systematic noise floor achieved by Kepler for quiet solar-type stars on transit-relevant timescales (R. L. Gilliland et al. 2011). The exact value of this noise floor needs to be refined and ultimately tested on-sky. To enable precise photometric observations of exoplanet transits, one of the sensors will have a broadband Kepler-like bandpass filter (nominally from 400–900 nm) to maximize the stellar flux rate, while being defocused slightly to enable better averaging over interpixel sensitivity effects. For the high photometric precision observations, care will be taken to enable the capability of observing and extracting data of nearby reference stars, leveraging lessons learned from the Kepler and TESS missions on cotrending basis vectors (e.g., M. C. Stumpe et al. 2012; J. M. Jenkins et al. 2016). Exposure time calculator and tools have been developed for the WCC and will be made available to the community in the near future.

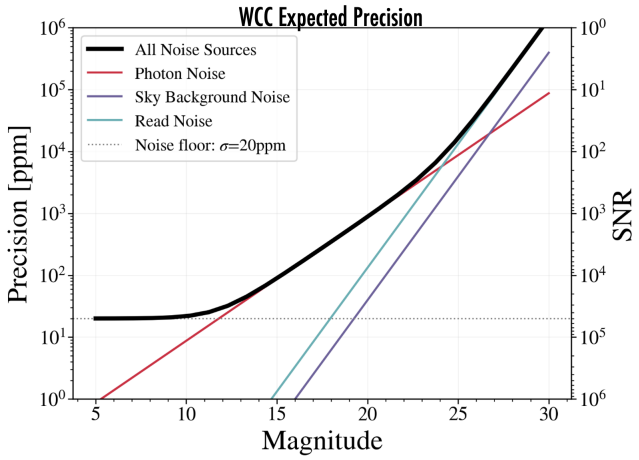

Figure 4. Expected photometric precision (black curve; left axis) in ppm and S/N (right axis) as a function of stellar magnitude as observed in the in-focus WCC *r* filter with the WCC in a 1 hr effective exposure. The contributions from different noise sources are highlighted: photon noise (red), sky background (purple), read noise (turquoise), and systematic noise floor (gray horizontal dashed line).

4.5. IFS

The IFS provides continuous wavelength coverage from 400–1700 nm—spanning more than two octaves—at spectral resolution $R \sim 100$–500. The IFS optical design, input fields of view, and expected detector trace locations are shown in Figure 5. The IFS offers two parallel fields: a narrow field (NF) with a $2\farcs3 \times 4\farcs6$ field of view with 40 mas spatial sampling, and a WF with a $4\farcs6 \times 8\farcs8$ field of view with 80 mas spatial sampling. The IFS has minimal moving parts for science observations to increase its reliability and calibration consistency.

The optical design builds on slicer integral-field designs from SNAP (G. Aldering et al. 2002; A. Ealet et al. 2006), WFIRST/Roman (G. Gao et al. 2017), and, most directly, ORKID-II (B. A. Pasquale et al. 2024). It consists of foreoptics, an image slicer integral-field unit (IFU), and a TMA spectrograph. The foreoptics relay the telescope focal plane to a reimaged focus at the IFU entrance, creating a slow beam to accommodate the slicer geometry and introducing 1:2 anamorphism to increase the S/N on the detector for faint continuum-source objects. A pupil image within the foreoptics enables calibration injection matched to the telescope illumination. The IFU employs a diamond-turned aluminum image slicer, with heritage from the DKIST solar telescope (T. Anan et al. 2024) and the INFUSE rocket-borne mission (E. M. Witt et al. 2021). The slicer consists of 58 slices for each of the NF and WF sky fields, reformatting the 2D field into a pseudoslit. The spectrograph uses an off-axis parabola collimator, a prism disperser for continuous wavelength coverage without order overlap, and a TMA to reimage the dispersed spectra onto the detector.

The detector is a Teledyne H4RG-10 with a 1700 nm cutoff, selected for its performance across the broad IFS bandpass. The median quantum efficiency exceeds 50% at 800 nm and 70% at 1200 nm, with goals of 60% and 80%, respectively. The detector is passively cooled to an operating temperature of 120 K to minimize dark current, and is expected to achieve a median dark current $\leqslant 0.01$ $e^- s^{-1} pix^{-1}$ with a goal of $\leqslant 0.001$ $e^- s^{-1} pix^{-1}$. The median correlated double sampling (CDS) read noise is $\leqslant 25$ e^-, with a goal of 20 e^-.

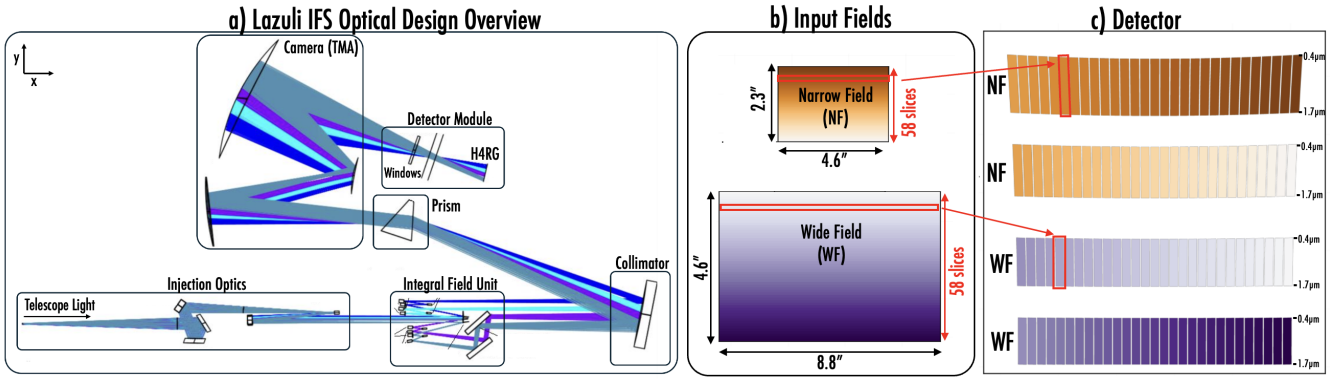

Figure 5. (a) Overview of the optical design of the Lazuli IFS, showing the injection optics, IFU, collimator, prism, the camera subsystem, and the detector module subsystem. (b) The input fields of view of the IFS, which is composed of a $2.''3 \times 4.''6$ NF, and a $4.''6 \times 8.''8$ WF. (c) Overview of the expected locations of the 116 traces (58 per subfield) as viewed on the 4096×4096 pixels of the H4RG-10 detector. The overview of the slices is generated by the `slicersim` code (M. Rigault et al. 2026).

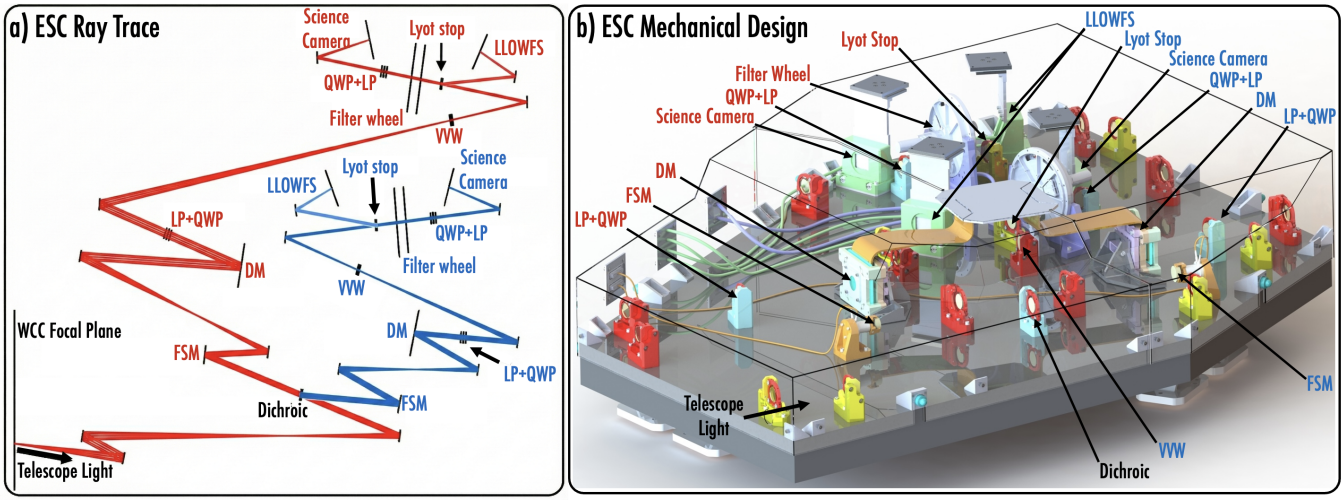

Figure 6. Preliminary optical ray trace and mechanical design of the ESC instrument. (a) Light enters from the bottom left where a dichroic splits the light into a red and a blue channel, followed by a piezo-electric FSM (PZT FSM; C. B. Mendillo et al. 2012) for fine guiding, 1K and 2K Boston Micromachines MEMS DMs for active wave front control, linear polarizer (LP) and quarter wave plate (QWP) for polarization filtering, charge-6 liquid-crystal polymer VVW plate coronagraph masks, reflective LLOWFS (C. B. Mendillo et al. 2023a), optional self-coherent camera modes (K. Z. Derby et al. 2023), selectable narrowband filters, and low-noise CMOS science cameras. (b) A composite optical bench supports ruggedized optics mounts, adapted from R. Huie et al. (2024), and a filter wheel is adapted from OSIRIS-REx OCAMS (B. Rizk et al. 2018). Baffles, covers, and electronics boxes are not shown, and components are artificially colored for emphasis. Computer-aided design (CAD) figure credit: H. Olivas and G. West. Coronagraph design concept developed by the University of Arizona.

The IFS is designed for high-precision spectrophotometry spanning up to 4 orders of magnitude in flux, enabled by comprehensive 2D and 3D calibration systems. The 3D calibration system injects light at the foreoptics pupil plane to match the telescope illumination, providing flat fields through the full spectrograph optical path. Wavelength calibration is achieved using a quartz–tungsten–halogen (QTH) lamp combined with a Fabry–Perot etalon and laser diode reference line. The 2D calibration system illuminates the detector directly via four LED sources spanning the IFS passband, enabling flux-dependent linearity corrections across the full dynamic range and characterization of detector regions receiving low flux from the spectrograph optics, such as near the gaps between slice projections. A calibration shutter mechanism enables dark exposures without thermal contributions from the telescope or sky. Together, these systems substantially reduce or eliminate the need for on-sky flat-field observations, which require astrophysical sources that are rarely sufficiently uniform for the precision required.

4.6. ESC

ESC (see Figure 6) is a high-contrast imaging system designed to enable direct imaging and characterization of exoplanets and circumstellar debris disks around nearby stars. The ESC design relies on many recent technological advances, leveraging progress in adaptive optics (AO) and coronagraph technology development on ground-based observatories (see review in L. Pueyo 2018), suborbital coronagraph missions (C. B. Mendillo et al. 2012; E. S. Douglas et al. 2018; C. B. Mendillo et al. 2020), and laboratory testbeds (for a summary review, see B. Mennesson et al. 2024). Particularly influential in the Lazuli ESC design have been the PICTURE-C mission (T. Cook et al. 2015; C. B. Mendillo et al. 2023b), the DeMi CubeSat (E. Douglas et al. 2021; R. E. Morgan et al. 2021), work at NASA's High Contrast Imaging Testbed Facility at JPL (J. T. Trauger & W. A. Traub 2007; G. Ruane et al. 2022; A. Potier et al. 2023), and the University of Arizona Space Coronagraph Optical Bench (SCoOB; E. R. Maier et al. 2020; D. Kim et al. 2021;

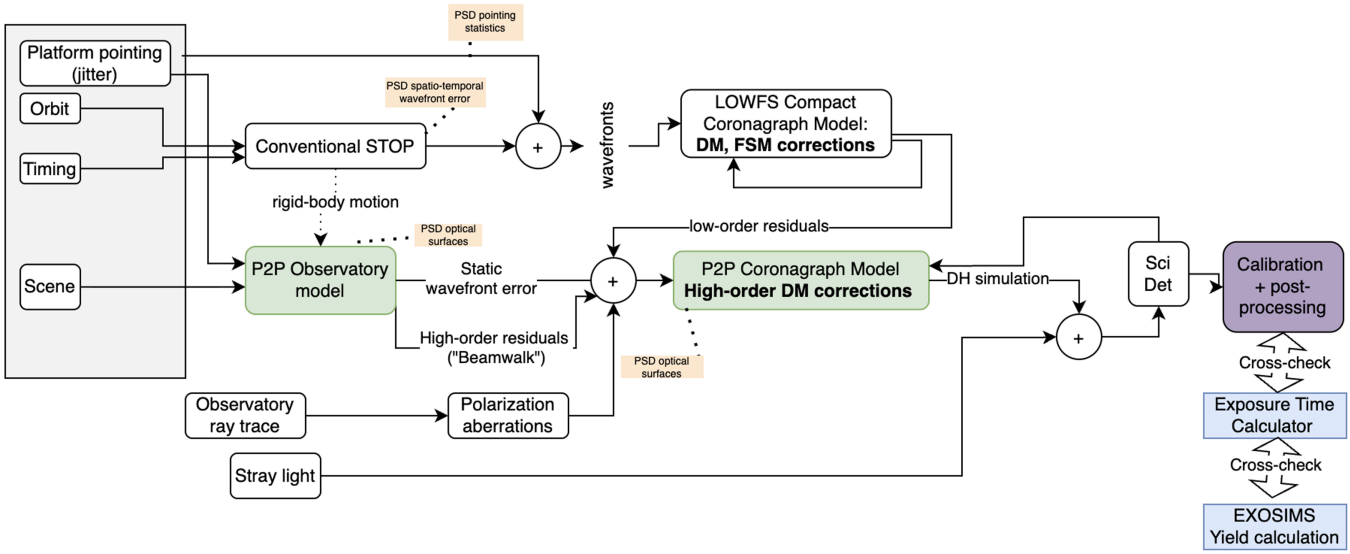

Figure 7. Planned simulation flow for modeling of Lazuli coronagraphic observations. Inputs on the left define the pointing environment, orbit, timing, and scene, which define the behavior of a STOP analysis and the inputs to the plane-to-plane (P2P) paraxial diffraction model. A LOWFS model defines what platform dynamic residuals can be controlled, which are then provided as inputs to the high-order DM corrections model, which includes HOWFS, the MEMS DM behavior, and wave front surface errors; outputs are combined as an intensity incident on the Science Detector (Sci Det), which then can be used as an input to postprocessing simulations, which can then be checked against exposure time estimates or used as inputs to the next iteration of the HOWFS model.

J. N. Ashcraft et al. 2022, 2024; K. Van Gorkom et al. 2022; K. Van Gorkom et al. 2024). The science yield of the high-contrast design will then be mapped leveraging community-developed tools such as EXOSIMS, the Exoplanet Open-Source Imaging Mission Simulator (D. Savransky et al. 2017). These efforts provide a strong technical foundation and substantially reduce development risk.

Building on these foundations, the Lazuli ESC employs a two-arm coronagraph design spanning 400–750 nm that requires minimal new technology development. The system combines 1K and 2K microelectromechanical system (MEMS) deformable mirrors (DMs; T. G. Bifano et al. 1997; E. S. Douglas et al. 2018; A. Potier et al. 2023), charge-6 vector vortex wave (VVW) plates in the focal plane (G. Serabyn et al. 2019). Together with a Lyot stop, the vortex wave plate forms a vector vortex coronagraph (VVC) (D. Mawet et al. 2010; G. Ruane et al. 2017, 2022). Finally, CMOS detectors and a software architecture derived from the MagAO-X instrument (J. R. Males et al. 2024a), which shares many common packages with other advanced ground-based AO projects (O. Guyon et al. 2018; N. Skaf et al. 2024), provide sensing and control to suppress speckles. Running proven AO software in Linux on industrial embedded computers with onboard graphics processing unit (GPU) acceleration greatly enhances the flexibility and shortens the time to deployment versus a traditional flight software development life cycle. The planned simulation flow for modeling Lazuli coronagraphic observations is shown in Figure 7.

Wave front sensing and control are implemented using a twofold approach to address a wide range of spatial and temporal frequencies. First, low-order aberrations, including pointing errors, are corrected using a Lyot low-order wave front sensor (LLOWFS) that uses light diffracted by the vortex focal-plane masks and reflected from the Lyot stop (G. Singh et al. 2015), an approach that has been optimized and demonstrated in relevant regimes (C. B. Mendillo et al. 2023a; K. Milani et al. 2025b). Even a well-corrected optical system with a VVC will have speckles of order 10^{-5} due to manufacturing errors; thus, a second, focal-plane speckle suppression step is required. This is achieved using half-focal-plane high-order wave front sensing (HOWFS) to generate a " dark hole" region of high contrast where the speckle intensity due to phase and amplitude errors is minimized (A. Give'on et al. 2007); see, for example, Figure 8. We have baselined the proven implicit-electric-field conjugation technique (S. Y. Haffert et al. 2023; K. Milani et al. 2023), which minimizes sensitivity to model errors and has been shown to provide 4 orders of magnitude of speckle suppression in 2% bandwidth with a comparable coronagraph (K. Van Gorkom et al. 2022, 2024). Other optional HOWFS modes to measure and/or stabilize the PSF are included, such as linear dark-field control (K. Miller et al. 2017) and a self-coherent camera mode for spatial variation of the speckle field in the dark hole (P. Baudoz et al. 2005; A. Potier et al. 2020; K. Derby et al. 2025). The SpaceVPX onboard compute system based on NVIDIA AGX Orin allows HOWFS operations to be performed onboard. The half-dark-hole approach provides high contrast and throughput without requiring the stringent high spatial frequency static surface smoothness of two-DM-in-series designs (J. Mazoyer & L. Pueyo 2017), at the expense of a concept of operations that requires multiple separate observations to perform 360° imaging around a single star. The onboard Linux computing environment further enables testing of alternative HOWFS algorithms, including adjoint methods (K. Milani et al. 2025a), linear dark-field control (K. Miller & O. Guyon 2016), and related approaches.

Early testing of this approach has demonstrated contrasts better than 10^{-8} in 5% or narrower bandwidths using existing hardware (K. Van Gorkom et al. 2024; K. Milani et al. 2025a). An in-vacuum laboratory-measured dark hole from the SCoOB testbed, in a configuration analogous to the red channel of Lazuli, is shown in Figure 8. Combining the coronagraph with an unobscured 3 m class telescope opens significant discovery potential for both exoplanet imaging and circumstellar disk studies while demonstrating several new technologies. To

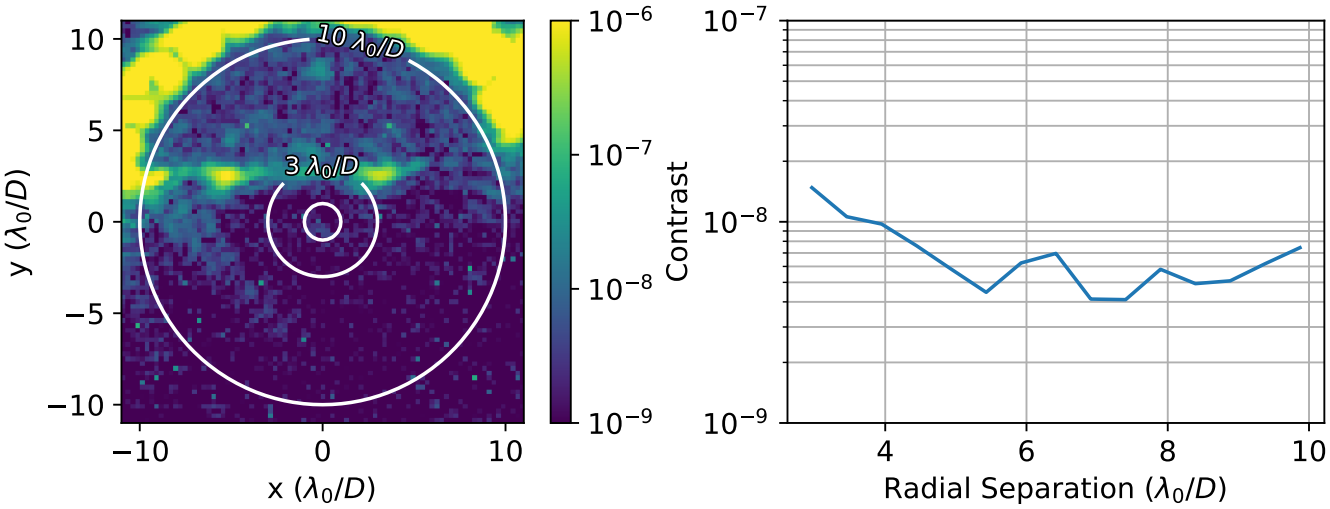

Figure 8. Measured contrast on the SCoOB testbed in vacuum in a 2% bandwidth centered at $\lambda_0 = 630$nm. The mean normalized intensity contrast in a D-shaped dark hole from 3 to $10\lambda_0/D$ is 5.8×10^{-8}. Adapted from K. Van Gorkom et al. (2024).

support performance prediction and system optimization, the team has been developing a range of tools to accelerate the end-to-end modeling framework, including GPU-accelerated angular spectrum methods for high-contrast imaging modeling (K. Milani et al. 2024) and post processing (P. M. S. Krishnanth et al. 2024) using CuPy (R. Okuta et al. 2017), extending `Batoid` (J. Meyers et al. 2019) for parallelized C++ ray tracing of complex surfaces for optical tolerancing to enable structural thermal optical performance (STOP) modeling (P. Nicolas et al. 2026, in preparation), and PyTorch implementations of Karhunen–Loéve postprocessing (C.-L. Ko et al. 2024). A single end-to-end contrast budget is used to track the contribution of instrument and observatory systematics, building on prior work from many teams (M. N'Diaye et al. 2013; C. B. Mendillo et al. 2017; B. Nemati et al. 2017, 2023; K. Van Gorkom et al. 2025). End-to-end simulations provide a means of verification and validation of the contrast budget terms and the planned coronagraphic observatory simulation flow (Figure 7), inspired by the Roman Coronagraph modeling approach (J. Krist et al. 2018), using power spectral density (PSD) representations of spatiotemporal error distributions as described in E. S. Douglas et al. (2023). Initial results of this approach will be published in E. S. Douglas et al. 2026 (in preparation). As the observatory design coalesces, statistically defined surfaces and temporal variations will subsequently be updated and/or replaced with as-built measured optical surface error maps and STOP time-series results.

5. Science Capabilities and Touchstone Use Cases

The Lazuli Space Observatory is designed with an instrument suite that enables access to regions of observational parameter space that remain poorly explored, particularly at the intersection of rapid response, stable spectrophotometry, and broad optical–NIR wavelength coverage. In this section, a set of touchstone use cases is presented to illustrate how Lazuli's design capabilities translate into high-impact science. The examples are organized around three high-priority science areas for Lazuli: time-domain and multimessenger astronomy (TDAMM; Section 5.1), stars and planets (Section 5.2), and cosmology (Section 5.3); they were selected both for their scientific importance and for the role they played in shaping key observatory requirements. While not exhaustive, these use cases highlight the breadth of studies enabled by Lazuli, ranging from high-cadence (∼5 ms) photometry with the WCC (e.g., X-ray binary time-lag measurements, searches for fast optical counterparts to fast radio bursts, and pulsar studies) to complementary cosmological probes (e.g., an independent H_0 measurement from strongly lensed SNe with the IFS) and multifaceted investigations of planet formation and evolution pathways.

5.1. TDAMM

When Lazuli starts science operations, it will join a suite of facilities dedicated to the pursuit of TDAMM.

This will include several wide-field surveys designed to systematically explore, for the first time, very short timescales (minutes—a day), including the Argus array (optical, N. M. Law et al. 2022), Rubin's LSST combined with other surveys such as the La Silla Schmidt Southern Survey (optical; A. A. Miller et al. 2025), ULTRASAT (UV; Y. Shvartzvald et al. 2024), and the Deep Synoptic Array (DSA; radio, G. Hallinan et al. 2019).

To fully exploit the scientific opportunities that these facilities will generate, including detailed studies of the earliest phases of transient evolution as well as the characterization of rare and/or currently unknown phenomena, a key bottleneck in the existing infrastructure is the capability to rapidly obtain follow-up photometry and spectroscopy.

To probe the evolution of fast-evolving transients in detail, a combination of rapid-response and sensitivity afforded by extremely large ground-based or large space-based observatories is required. While planned/proposed missions will cover this combination of capabilities at other wavelengths (e.g., UVEX, S. R. Kulkarni et al. 2021; AXIS, C. S. Reynolds et al. 2023), no $\gtrsim$1 m space-based observatory planned in the next decade covers optical–NIR spectroscopy.

Lazuli, with its large aperture and a mission operations concept designed to be flexible and responsive, is expected to enable follow-up observations of the faintest, fast-evolving transients at scale, thereby opening up a new part of parameter space for systematic exploration. Lazuli's concept of operations is structured to enable response times to community

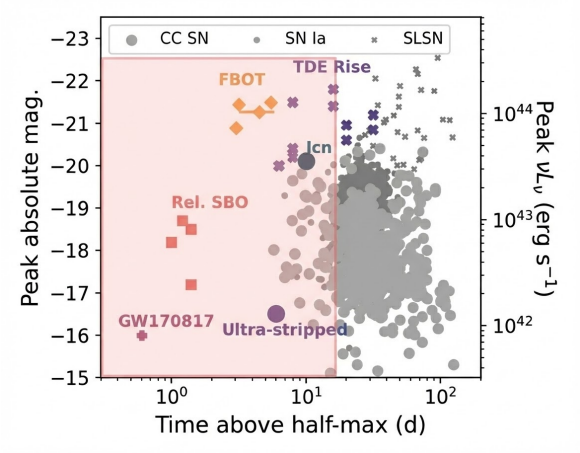

Figure 9. Lazuli provides new opportunities to study faint and fast-evolving phenomena. The red box highlights where Lazuli's rapid response and sensitivity will open up new parameter space for systematic exploration. Even for the faint end (absolute magnitude of –15), Lazuli's distance horizon for spectroscopy of fast-evolving transients is $\lesssim$1 Gpc. Highlighted sources include GW170817, the kilonova counterpart to a BNS merger; relativistic SN shock-breakout (rel. SBO) events; FBOTs; and rapidly evolving (ultra) stripped envelope SNe such as SNe Icn. Normal SNe are shown in gray. The x-axis shows how much time a source spends above half of its maximum brightness, a proxy for whether its evolution is fast or slow. Figure adapted from S. R. Kulkarni et al. (2021).

target of opportunity (ToO) requests on timescales shorter than 4 hr (from trigger submission to open shutter on target), with a goal of 90 minutes. In addition to rapid-response, Lazuli will have the capability to perform high-cadence (down to ∼hours, in principle) monitoring over timescales of weeks with minimal interruptions, providing regular sampling of transient evolution that is very hard to reliably achieve from the ground.

5.1.1. Fast Transients

Over the past two decades, a range of fast-evolving astrophysical phenomena with characteristic timescales of milliseconds to weeks has been discovered. These include fast radio bursts; optical and IR flaring from X-ray binaries and magnetars; luminous, UV and X-ray-bright fast transients that potentially could be powered by the tidal disruption (and in some cases detonation) of a white dwarf around an intermediate-mass black hole (BH; see S. Gezari et al. 2026, in preparation, for a detailed analysis); and fast transients such as SN shock-breakout (SBO) and jet-driven events from massive stars, among others (Figure 9). Despite growing interest, the number of well-characterized sources remains small, and in several cases robust classifications have yet to be established.

These events occupy an extreme corner of parameter space; they are intrinsically rare, distant, and often too faint and/or short-lived for systematic multiwavelength follow-up. With its combination of rapid response, deep optical–NIR imaging and low-resolution spectroscopy, and flexible scheduling, Lazuli will overcome the main bottlenecks limiting exploration of this parameter space, enabling both routine classification and detailed physical interpretation of these rare phenomena. For reference, in a 6 hour observation with the IFS, Lazuli can deliver S/N > 5 over most of the covered wavelength range for a peak absolute magnitude of –15 at a distance of ∼1 Gpc ($z \sim 0.2$). For a peak absolute magnitude of –22, the distance horizon for spectroscopy extends out to $z \sim 3$.

In addition to the exploration of this poorly understood part of parameter space, we highlight a number of science cases where Lazuli is expected to provide new insights and/or highly complementary capabilities compared to existing facilities. These scenarios showcase the power and potential of Lazuli to improve our understanding of the dynamic Universe and have a broad impact on time-domain science.

5.1.2. Gravitational-wave Follow-Up

Gravitational-wave detections from merging neutron stars (NSs) and BHs have opened up a new window on the Universe. The most likely detectable electromagnetic counterpart to a binary NS (BNS) merger is a fast-evolving, faint transient with potential emission from gamma rays through X-ray, UV, optical, NIR, submillimeter, and radio wavelengths. This emission encodes fundamental information on the physics of dense matter, the formation of heavy elements, and the nature of the merger remnant. In addition, NS–BH mergers may also produce fast-evolving and faint kilonova emission (K. Kunnumkai et al. 2025a); this emission has not yet been detected but occupies the parameter space in which Lazuli will excel.

We show the multiband light curves of the kilonova counterpart to GW170817 from P. S. Cowperthwaite et al. (2017), R. Chornock et al. (2017), S. Valenti et al. (2017), N. R. Tanvir et al. (2017), I. Arcavi et al. (2017), E. Pian et al. (2017), E. Troja et al. (2017), S. J. Smartt et al. (2017), I. Andreoni et al. (2017), Y. Utsumi et al. (2017), M. M. Kasliwal et al. (2017), P. A. Evans et al. (2017), M. R. Drout et al. (2017), M. Soares-Santos et al. (2017) in Figure 10, shifted to a distance of 600 Mpc (which is the median expected distance for BNS mergers for which counterparts will be detectable in the fifth LIGO/Virgo/KAGRA observing run, e.g., K. Kunnumkai et al. 2025b), together with estimates for the limiting magnitudes of Lazuli IFS spectroscopy and WCC imaging. We also overplot two example kilonova models (the radioactive decay model of M. M. Kasliwal et al. 2017 and the shock-cooling + boosted radioactive decay model of V. A. Villar et al. 2017) to highlight the discriminating power of early observations.

Lazuli can provide continuous 400–1700 nm spectroscopy for classification and characterization from the first hours up to ∼7 days postmerger at 600 Mpc. The distance horizon for Lazuli spectroscopy for a GW170817-like kilonova at peak is ≈ 1 (1.5) Gpc; this volume encompasses >85% of all BNS mergers expected to be detected by the LIGO–Virgo–KAGRA observatory during its next O5 observing run (K. Kunnumkai et al. 2025b).

The most model-constraining phases of kilonovae occur within the first hours to days after the event (I. Arcavi 2018), when the emission is rapidly evolving, relatively blue, and directly shaped by the composition, velocity, and geometry of the ejecta. Capturing this early light requires the combination of fast response, regular high-cadence monitoring, and sensitivity that no existing or planned space observatory is designed to provide at scale.

Lazuli's rapid response will provide constraining power to differentiate between different kilonova components such as shock-heated material, disk winds, and lanthanide-rich ejecta, thereby constraining the production of the heaviest elements in the Universe (e.g., D. Kasen et al. 2017; B. D. Metzger 2020). Lazuli's broad wavelength coverage and stable

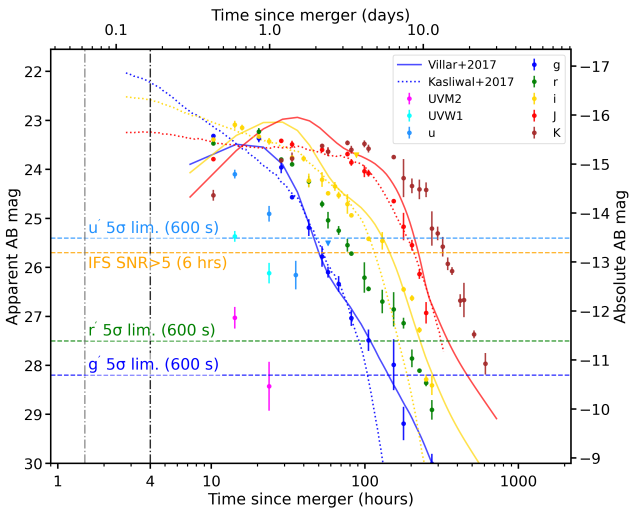

Figure 10. Multiband light curves of the kilonova counterpart to the BNS merger GW170817, shifted to a distance of 600 Mpc. Lazuli's rapid response will enable very early spectroscopic and photometric constraints of future kilonovae, where the model predictions diverge and hence discriminating power is largest. It can obtain broadband light curves and spectroscopy for nearly all BNS mergers out to 1–1.5 Gpc, provided that the correct counterpart is identified in a timely manner. The vertical dashed–dotted lines show the 4 hr requirement (black) and 90 minute goal (gray) for ToO response time. Horizontal colored lines indicate the 5σ limiting magnitude for WCC photometry in the *u*, *g*, and *r* bands (light blue, dark blue, and green respectively), and the limiting magnitude to obtain a $S/N \gtrsim 5$ spectrum with the IFS (orange).

spectrophotometry are ideally suited to identifying key spectral features, including potential signatures of r-process species at wavelengths that are inaccessible from the ground. At later times (days to weeks), Lazuli can track the potential emergence of the afterglow from an off-axis jet, providing crucial information about jet structure, viewing angle, and the physics of relativistic outflows (e.g., E. Nakar & T. Piran 2017). Together, and in combination with other multiwavelength rapid-response facilities, these measurements will enable a detailed reconstruction of the merger: from the composition of the ejecta and the fate of the remnant to the geometry and energetics of any associated jet. A more detailed analysis of Lazuli's capabilities for multimessenger astronomy will be presented in K. Kunnumkai et al. 2026 (in preparation).

5.1.3. FBOTs

Luminous FBOTs (LFBOTs; e.g., S. J. Prentice et al. 2018) further exemplify the scientific opportunities with Lazuli. These events are characterized by bright ($>10^{43}$ erg s^{-1}) emission, spanning radio through X-ray bands (e.g., R. Margutti et al. 2019). Their rapid evolution, including continuum cooling, the emergence (or lack thereof) of spectral features indicating high-velocity ejecta and/or shock interaction features (e.g., R. Margutti et al. 2019; D. A. Perley et al. 2019), holds clues to their progenitors, the explosion geometry, and the nature of the (tentative) central engine.

The 400–1700 nm IFS coverage will enable detailed tracking of the optical–NIR spectral energy distribution (SED) evolution, while simultaneously capturing the emergence and temporal evolution of spectral features. Together with UV from facilities such as HST, X-ray, and radio observations, Lazuli can provide the high-cadence, panchromatic data required to break model degeneracies. One illustrative example is the persistent NIR excess observed in AT2018cow, whose origin remains uncertain; it has been attributed to either (i) dust echoes of circumstellar material—offering insight into the mass-loss history and nature of the progenitor (e.g., B. D. Metzger & D. A. Perley 2023)—or (ii) reprocessing by a dense outflow, which could constrain outflow geometry, energetics, and the nature of the central engine (e.g., C. Chen & R.-F. Shen 2025).

Equally transformative is Lazuli's ability to characterize the minute-scale optical flares such as those recently discovered in the LFBOT AT2022tsd (A. Y. Q. Ho et al. 2023), with a typical peak magnitude of –20 (AB mag) in the optical bands. Lazuli will have the sensitivity to measure flare duty cycle, energetics, and substructure on timescales of tens of seconds with the WCC. In addition, it will be capable of time-resolved spectroscopy on 1–2 minute timescales to detect color changes and continuum shape variations for sources out to $z \sim 1$ ($S/N \gtrsim 5$ across the wavelength range), providing direct constraints on the origin of this emission (synchrotron, magnetar-powered, or jet-driven). A more detailed summary of the wide range of time-critical and transient science cases that Lazuli's capabilities will enable can be found in T. Wevers et al. (2026).

5.2. Stars and Planets

Planets and their host stars evolve in tandem, from the earliest stages of planet formation through main-sequence evolution, potential habitability, and eventual dynamical or radiative disruption. The following subsections describe the science considerations that most strongly influenced the selection and design of Lazuli's instrument capabilities for characterizing stars, exoplanets, and our own solar system. These investigations are expected to make use of all three Lazuli instruments (ESC, WCC, and IFS), operating in complementarity with TESS, JWST, HST, Roman, PLATO, Ariel, and other current and upcoming facilities.

5.2.1. Direct Imaging of Habitable Zones, Giant Planets, and Circumstellar Disks with the ESC

The drive to deepen our understanding of Earth's history, climate, and uniqueness in the Universe motivates the search for other stellar systems and a broader understanding of the solar system's context within the Galaxy. Exploring the formation, composition, and dynamics of planets leads to general conclusions about the occurrence rates of exoplanets and robust physical measurements of specific planets that test local models. Large samples are required for statistically robust measurements, such as the occurrence rate of short period planets around FGK stars inferred by Kepler transit observations (e.g., J. N. Winn & D. C. Fabrycky 2015; M. Kunimoto & J. M. Matthews 2020, and many others) or wide-orbit planet occurrence rates measured by microlensing surveys such as the Optical Gravitational Lensing Experiment (OGLE; R. Poleski et al. 2021) or the upcoming Roman Microlensing Survey (M. T. Penny et al. 2019; A. P. Boss 2025).

However, getting to large numbers of planets requires searching around dim, distant stars in addition to bright, nearby hosts. Such surveys do not tend to discover suitable planets for follow-up observations that probe physical properties at the spatial scales of a planetary radius or temporal scales

shorter than a human lifespan. Transit surveys of brighter stars (e.g., with TESS; N. M. Guerrero et al. 2021) provide a better sample for follow-up with transit spectroscopy, while radial velocity and direct imaging surveys of nearby stars are the most direct ways to find planets that can be characterized in detail. Ground-based observations with 5–10 m class telescopes equipped with AO have resolved young, warm, freshly formed or adolescent giant planets in emission (e.g., B. P. Bowler 2016) as well as large numbers of bright circumstellar disks (e.g., H. Avenhaus et al. 2018; T. M. Esposito et al. 2020). Extending extreme AO technology to the upcoming 30 m class telescopes (O. Guyon 2018; M. P. Fitzgerald et al. 2022; R. Jensen-Clem et al. 2022; G. Chauvin 2024; J. R. Males et al. 2024b) is expected to lead to the imaging of Earth-like planets around nearby M dwarf stars. For most hypothetical exoplanets around FGK stars, reflected light is 10^{7}–10^{10} times dimmer than the host star (the "star–planet flux ratio"), and circumstellar debris disks span an even larger dynamic range of resolution element to host star contrast. The Coronagraph Instrument aboard the Nancy Grace Roman Space Telescope, launched in 2026, with multiple active optics, is likely to take our first image and spectrum of a Jupiter analog (R. E. Lupu et al. 2016; N. E. Batalha et al. 2018; V. P. Bailey et al. 2023). To image a statistically significant sample of Earth-like planets around Sun-like stars and search for life in their atmospheres, the Astro2020 Decadal Survey recommended a UV–optical–IR exoplanet imaging mission, now known as the HWO, with a ∼6.5 m coronagraphic space telescope launched in the early 2040s (National Academies of Sciences et al. 2021). A significant gap in flight-demonstrated starlight suppression still remains between the current state of the art (HST and JWST) and what is needed for Sun-like stars. Lazuli addresses that gap. It uses technologies that are complementary to those aboard Roman (e.g., N. J. Kasdin et al. 2020; E. Cady et al. 2025) and has similar projected performance with some advantages, due to the 3 m telescope, and limitations, due to the limited number of modes; most notably, Lazuli's coronagraph concept omits spectroscopy.

The Lazuli mission's flexibly scheduled, high-throughput 3 m class coronagraphic imaging goal sensitivity of $\leqslant 10^{-8}$ planet–star flux ratios is expected to provide unprecedented detectability of debris disks and giant exoplanets around nearby stars, some of which could be followed up spectroscopically by Roman or HWO (see Figure 11). These contrast ratios, combined with the expected resolution and throughput of the Lazuli telescope aperture, also enable immediate reconnaissance of the habitable zones of nearby stars, with a sensitivity commensurate with detections of giant planets and (bright) exozodiacal dust. Detection (or nondetection) of giant planets will provide insights into their occurrence and atmospheric properties, and potentially reveal exomoons (M. A. Limbach et al. 2024; K. Wagner et al. 2025). Further, constraining the orbital locations and architectures of massive planets around the nearest stars will help identify which systems are dynamically compatible with hosting terrestrial planets in the habitable zone (e.g., S. R. Kane 2025), which could later be observed with future direct imaging capabilities such as HWO and the Large Interferometer for Exoplanets (LIFE; S. P. Quanz et al. 2022).

Coronagraph performance depends on stellar magnitude, so early searches are expected to be a quick survey of bright stars

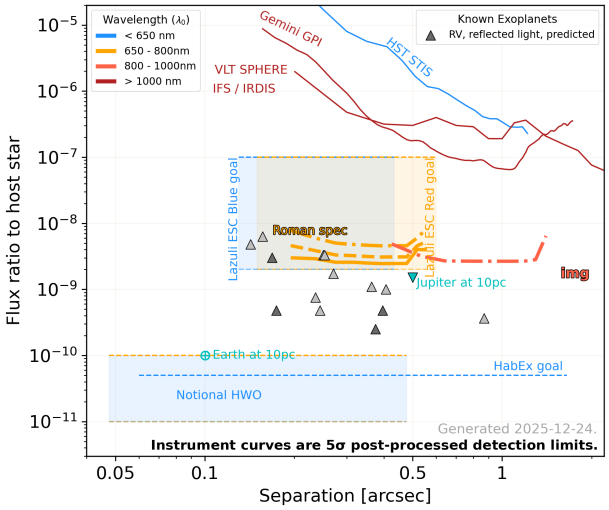

Figure 11. Lazuli ESC goal planet–star flux ratio versus distance from the star on the sky compared to Roman and HWO, 5σ final sensitivity curves adapted from *DI-flux-ratio-plot* (V. Bailey and S. Hildebrandt; https://github.com/nasavbailey/DI-flux-ratio-plot). Compared to Roman, Lazuli's smaller inner working angle goal of 0.″12 will enable additional detections and photometry of exoplanets across more of their orbital phase function. Roman will be able to follow up Lazuli discoveries spectroscopically (dashed yellow lines). HWO's notional sensitivity requirements are shown in the bottom left (blue shaded area, approximately adapted from C. C. Stark et al. (2024) and other sources) and reflect 2 orders of magnitude improvement in postprocessed sensitivity.

along with repeated observations of a few cornerstone targets to maximize the multivisit search completeness around a subset. Figure 11 shows the flux ratio sensitivity expected in context with Roman and HWO. Jupiter analogs around Sun-like stars and systems with known radial velocity planets (upward-pointing triangles) are expected to be excellent targets at these sensitivities. The Roman Coronagraph's early science is likely to inform Lazuli's target selection strategy. Where Roman and Lazuli overlap, Lazuli will provide shorter wavelength measurements and potentially more complete phase functions closer to host stars. Lazuli's reconnaissance of bright systems will provide new, deep measurements of the scattered light background from exozodiacal dust (e.g., A. Roberge et al. 2012; E. S. Douglas et al. 2022; S. Ertel et al. 2025) and the presence of giant planets around many potential HWO targets. Future work to maximize the revisit cadence (e.g., C. M. Guimond & N. B. Cowan 2019; L. Pogorelyuk et al. 2022; M. Bruna et al. 2023), target selection (e.g., using improved priors or survey optimization with EXOSIMS), filter selection (e.g., N. E. Batalha et al. 2018), and develop optimal postprocessing and speckle subtraction techniques that leverage onboard telemetry and speckle diversity (e.g., A. Amara & S. P. Quanz 2012; R. Soummer et al. 2012; M. Ygouf et al. 2015; B. Ren et al. 2018; J. D. Long et al. 2024; M. J. Bonse et al. 2025; C. L. Page et al. 2025) while following best practices for leveraging artificial intelligence to science data analysis A. Crilly et al. (2025).

5.2.2. Exoplanet Transits with the WCC

The WCC is being designed to enable the detection and characterization of transiting exoplanets, including Earth analogs—i.e., ∼1 $R_{\oplus}$ planets orbiting within the habitable

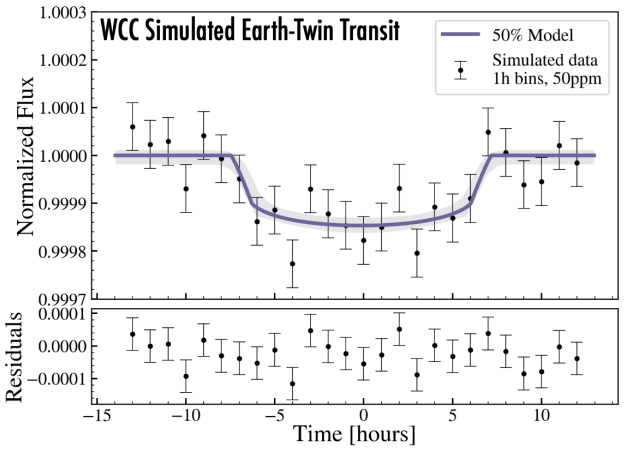

Figure 12. Expected transit of an Earth-twin around a Sun-like star as observed with the WCC, assuming the WCC achieves its 50 ppm precision in 1 hr effective integration bins observed for two transit durations, or about 26 hr. The median model from a best-fit Markov Chain Monte Carlo simulation (purple line) and corresponding 1σ credible interval and associated residuals are shown.

zones of solar-type stars. An Earth–Sun analog produces a transit depth of ∼80 ppm and a transit duration of approximately 13 hours. Achieving a statistically significant detection of such events therefore requires an effective photometric precision of ∼50 ppm in one hour of integration (see Figure 12), a performance level that the Lazuli system and the WCC are explicitly aiming to achieve.

To achieve this precision, one WCC sensor will operate in a defocused mode, allowing the stellar PSF to be distributed over many pixels. This approach mitigates the impact of interpixel sensitivity variations and reduces sensitivity to pointing jitter and guiding errors. As discussed in Section 4.4, this sensor will employ a broad, Kepler-like bandpass to maximize photon throughput and thereby minimize photon noise. In addition, the wide field of view of the WCC detectors ensures the presence of multiple nearby reference stars, enabling differential photometry to correct for spacecraft- and detector-related systematics.

This photometric capability enables a broad range of investigations of transiting exoplanets. One application could be a targeted survey of Earth-sized and habitable-zone planets discovered by Kepler (W. J. Borucki et al. 2010), K2 (S. B. Howell et al. 2014), TESS (G. R. Ricker et al. 2015), and the upcoming PLATO mission (H. Rauer et al. 2014). Repeated high-precision transit observations can refine orbital ephemerides, improve constraints on planetary radii and densities, and reduce uncertainties in the occurrence rate of terrestrial habitable-zone planets, $\eta_{\oplus}$, around nearby solar-type stars (S. Bryson et al. 2025; R. B. Fernandes et al. 2025). The effectiveness of such a survey in constraining $\eta_{\oplus}$ will be described in detail in an upcoming publication (M. A. Al Zaman et al. 2026, in preparation).

Beyond Earth analogs, the WCC's photometric precision will enable a wide range of additional exoplanet investigations. These include detailed photometric characterization of high-value transiting systems; the detection of orbital decay through long-baseline, high-precision transit timing measurements (e.g., K. C. Patra et al. 2017); searches for transiting exomoons via transit timing variations (e.g., D. M. Kipping 2009) and/or detection of moon transits (e.g., A. Teachey & D. M. Kipping 2018); the detection of additional planetary companions through transit timing variations (e.g., M. J. Holman & N. W. Murray 2005); and constraints on planetary obliquities and stellar surface properties through the analysis of starspot-crossing events during transit (e.g., P. A. Nutzman et al. 2011; R. Sanchis-Ojeda & J. N. Winn 2011).

5.2.3. Spectroscopy of Transiting Planet Atmospheres

The Lazuli IFS will have the unique capability to perform space-based high-precision spectroscopy of transiting exoplanets covering the continuous wavelength region from 400–1700 nm. This wavelength region includes key spectroscopic features of titanium and vanadium oxides (TiO, VO), alkali metals (Na, K), water vapor (H_2O), methane (CH_4), and/or hazes. While many previous ground-based surveys have focused on the alkali metals elements, and HST and JWST spectroscopic observations have detected alkali metals and oxygen-bearing and carbon-bearing molecules in many planets, Lazuli may be the first to simultaneously measure the haze slope, Na, K, and water vapor. These combined abundance measurements will constrain the mass–metallicity relation first discovered from the solar system's carbon abundance (e.g., L. Kreidberg et al. 2014; S. K. Atreya et al. 2022) to the sodium, potassium, and water only hinted at in previous studies that examine the alkalis and water vapor from different sources (e.g., L. Welbanks et al. 2019; Q. Sun et al. 2024). The Lazuli orbit allows continuous time-series spectroscopy without interruptions by Earth eclipses or day/night temperature swings that can introduce time-dependent systematics and gaps.

Figure 13 shows a simulation of an exoplanet transmission spectrum of a WASP-39 b–like planet (i.e., same brightness and host star spectrum) using a PICASO version 2.2.1 (N. E. Batalha et al. 2019) atmospheric model with no clouds or hazes. We also show a hazy model with a Rayleigh scattering cloud with a reference optical depth of 0.05, wavelength of 250 nm and power-law slope of 4.5. We simulate the expected errors for two transits of this planet, assuming equal in-transit and out-of-transit exposure time. To calculate the expected S/N, we use the `slicersim` package version 0.26.0 (M. Rigault et al. 2026) with default instrument parameters, the NF, 12 groups up the ramp with 1 frame per group, a 5400 K, [Fe/H]=0, log(g)=4 host star model (F. Castelli & R. L. Kurucz 2003; STScI Development Team 2013) with a J magnitude of 10.67.

Figure 13 also shows the existing data from JWST NIRISS SOSS (A. D. Feinstein et al. 2023), JWST NIRSpec PRISM (Z. Rustamkulov et al. 2023), HST WFC3 (H. R. Wakeford et al. 2018), and an Ariel simulation from Q. Changeat et al. (2025). While JWST, HST, and Ariel all cover the molecular features of hydrogen-bearing and oxygen-bearing molecules, the Lazuli IFS will bridge the visible and NIR spectra with a wide simultaneous bandpass. This mitigates against variations from epoch to epoch due to stellar activity that can change the transmission spectrum due to the transit light source effect (e.g., B. V. Rackham et al. 2019).

Lazuli should have access to a wide variety of planets from small terrestrial planets to giant planets shown in Figure 13 (panel (b)). A stripe subarray mode that only reads out a subsection of the detector with all 32 output channels on one row of slicer projections (projections visualized in Figure 5)

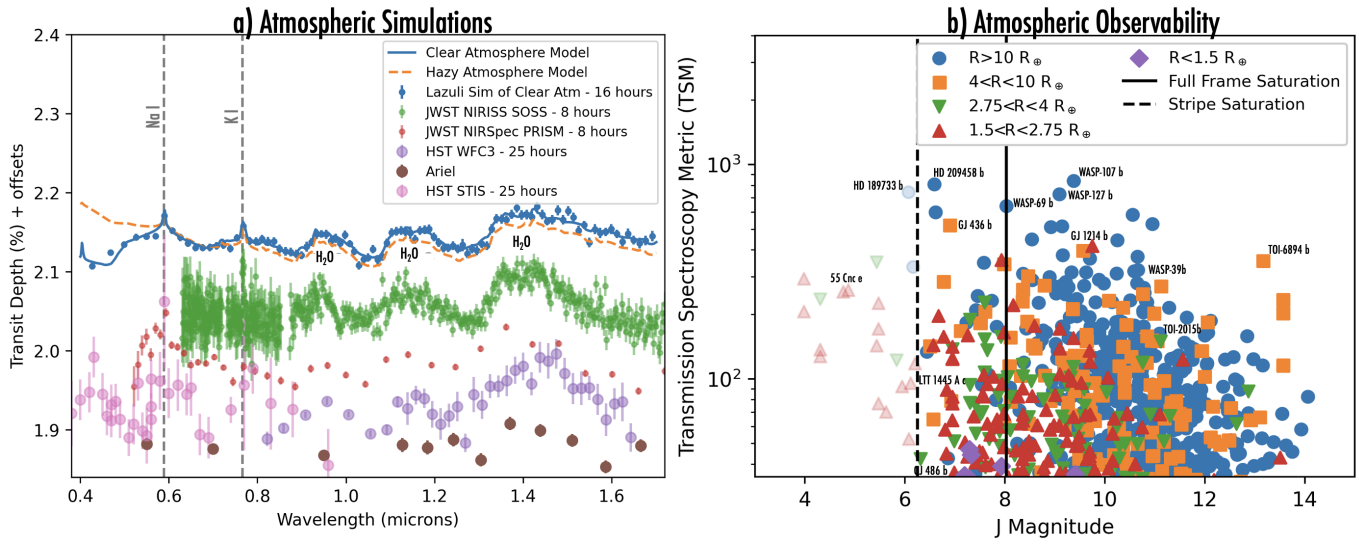

Figure 13. (a) A simulated transmission spectrum of a WASP-39 b–like exoplanet using `PICASO` (N. E. Batalha et al. 2019) and `slicersim` (M. Rigault et al. 2026). The Lazuli IFS spectra (blue data points) span the information-rich optical wavelengths sensitive to hazes, and Na and K to the NIR water-dominated absorption bands. This complements the IR capabilities of JWST and Ariel and enables seamless combinations of panchromatic spectra from the visible to NIR. b) Exoplanet systems fainter than the subarray saturation limit (dashed vertical line) will be accessible for transmission spectroscopy, including terrestrial, sub-Neptune, and giant exoplanets.

will allow observations of targets as bright as $J \approx 6.3$ without saturation, depending on the details of the final optical design. This subarray mode will also increase the efficiency of observations near the full-frame saturation limit at $J \approx 8.0$ from 33% (2 groups) to 91% (10 groups). A deeper analysis of Lazuli IFS transmission spectroscopy, including the efficacy of retrievals at various transmission spectroscopy metric thresholds and the resulting accessible exoplanet parameter space, is forthcoming (J. Pero et al. 2026, in preparation).

5.2.4. Characterizing Hα Emission from Accreting Protoplanets with the WCC

The youngest directly imaged exoplanets have been discovered while still embedded within their natal protoplanetary disks. Such "protoplanets" produce bright Hα emission as a consequence of ongoing accretion, making them visible against scattered light from the disks at contrast levels of $\sim 10^{-4}$ (see, e.g., C. Plunkett et al. 2025 and references therein). Comprehensive surveys with ground-based telescopes have hunted for accreting protoplanets in transitional disks (K. B. Follette et al. 2023), which show dust-depleted gaps and cavities in submillimeter continuum emission (S. M. Andrews et al. 2011) and optical-through-IR light (A. Garufi et al. 2018). Since the LOS extinction is lower in the gaps and cavities, Hα point sources are expected to be more distinct in these regions (F. Alarcón et al. 2024). However, to date only three sources have been confidently detected, due to challenges with subtracting background disk structure: PDS 70b (M. Keppler et al. 2018; K. Wagner et al. 2018), PDS 70 c (S. Y. Haffert et al. 2019), and WISPIT 2b (L. M. Close et al. 2025a).

Recent campaigns to observe accreting protoplanets with HST/WFC3 have demonstrated the power of using a wide-field camera on a space telescope for high-contrast imaging without a coronagraph (Y. Zhou et al. 2021, 2025). The improvement in PSF stability from space has also aided in distinguishing between true point source emission and scattered light artifacts from other substructure within the protoplanetary disks (Y. Zhou et al. 2022, 2023). With this in mind, the Lazuli WCC will carry a narrowband Hα filter, enabling $\sim 0\farcs1$–$0\farcs3$ postprocessing resolution that matches the radial locations of dust substructures that are resolved in submillimeter emission (S. M. Andrews et al. 2018; F. Long et al. 2018, 2019). Together with telescope roll angles of $>10^{\circ}$ for space-based angular differential imaging, these capabilities will enable (a) characterization of accretion variability from protoplanets detected from the ground (see also L. M. Close et al. 2025b; Y. Zhou et al. 2025) and (b) potential surveys to discover new point sources, with target selection guided by ever-increasing theoretical and observational knowledge of disk evolution and radiative transfer (Y. Aoyama et al. 2018; F. Alarcón et al. 2024; G. Cugno et al. 2025). A detailed exploration of how Lazuli WCC observations can untangle accreting protoplanets from background disk substructure is ongoing (C. Schneider et al. 2026, in preparation).

5.2.5. Solar System Spectroscopy with the IFS

Lazuli will also have the capability for nonsidereal tracking to resolve moving targets within the solar system while minimizing blurring across the detectors. The observatory baselines nonsidereal tracking capabilities of up to 30 mas s^{-1} and a goal of up to 60 mas s^{-1} that are expected to enable observations of the giant planets and their moons, comets, asteroids, Centaurs, and other Kuiper Belt objects (B. J. Holler et al. 2018). Together with the IFS spectral coverage from 400 to 1700 nm at $R \sim 100$–500, these capabilities are expected to reveal both water ice and mineral absorption features on targets spanning a wide range of diameters and orbital distances.

5.3. Cosmology

The discovery of the expanding Universe initiated the field of observational cosmology, which aims to understand the state, dynamics, and constituents of the Universe as traced by

astrophysical observables such as luminosity distance and cosmological redshift. The expansion of the Universe was discovered using Cepheid variable stars (H. S. Leavitt & E. C. Pickering 1912; E. Hubble 1929), and the discovery that the expansion is currently accelerating was made using Type Ia SNe (SNe Ia; S. Perlmutter et al. 1999; A. G. Riess et al. 1998). Both types of measurements, which helped establish the current standard model of cosmology (ΛCDM), are, with improved statistical uncertainties, now beginning to show surprising evidence for a more complicated model.

The combination of SNe Ia (D. Brout et al. 2022; DES Collaboration et al. 2024; D. Rubin et al. 2025b), baryon acoustic oscillations (BAOs; A. G. Adame et al. 2025; DESI Collaboration et al. 2025) and the cosmic microwave background (CMB) power spectrum (Planck Collaboration et al. 2020) imply an unusual dark energy time variation, while the comparison of the Hubble constant inferred from this CMB measurement with that inferred from local measurements currently disagree (S. A. Uddin et al. 2024; A. G. Riess & L. Breuval 2024).

We describe how the capabilities of the Lazuli Space Observatory are well suited to advance our understanding of the Universe through observations of SNe Ia, Cepheid variables, and strong gravitational lensing of SNe.

5.3.1. SNe Ia Cosmology

SNe Ia have long been prized as cosmological probes due to their high intrinsic luminosity ($M_B \sim -18$ mag) coupled with the ability to standardize their brightnesses either from parameters derived from their light curves (M. M. Phillips 1993; A. G. Riess et al. 1996; R. Tripp 1998) or from their spectra (H. K. Fakhouri et al. 2015; K. Boone et al. 2021a; G. Stein et al. 2022; C. Ganot et al. 2026). Combining these standardized brightnesses with redshifts allows the expansion history of the Universe to be measured out to $z \sim 2$ (e.g., DES Collaboration et al. 2024; D. Rubin et al. 2025b).

The recent surprising indications of time-varying dark energy put a new emphasis on trustworthy SN distance measurements, since it now becomes particularly important to ensure that both the statistical significance and systematic uncertainties are securely differentiating such time variation from a static dark energy, and then providing reliable indicators of the nature and timing of the variation. For this purpose, it is now possible to employ stronger standardization methods built on spectrophotometry, which, while more time-intensive, can enhance the major new surveys that discover SNe Ia, to accomplish the best currently possible measurements of the expansion history of the Universe over the past two-thirds of its existence.

The capabilities and timing of the Lazuli IFS will enable it to spectrophotometrically measure SNe Ia discovered by other forefront observatories, including the Roman Space Telescope High Latitude Time Domain Survey (HLTDS) (Roman Observations Time Allocation Committee & Core Community Survey Definition Committees 2025) and the Vera Rubin Observatory's Deep Drilling Fields (DDFs) and Wide Fast Deep (WFD) Survey (Ž. Ivezić et al. 2019; F. B. Bianco et al. 2022; Rubin's Survey Cadence Optimization Committee et al. 2025). Such unified spectrophotometric measurements with broad and uniform wavelength coverage will avoid any discontinuities that might otherwise spring from the cross calibration of different photometric systems of the discovery surveys, improving the results for the entire community. Figure 14 illustrates the expected Lazuli IFS performance for a representative $z = 1$ SN Ia spectrum. Figure 15(b) shows the visibility of each of the Rubin DDFs and the Roman HLTDS fields throughout one possible year of Lazuli operations.

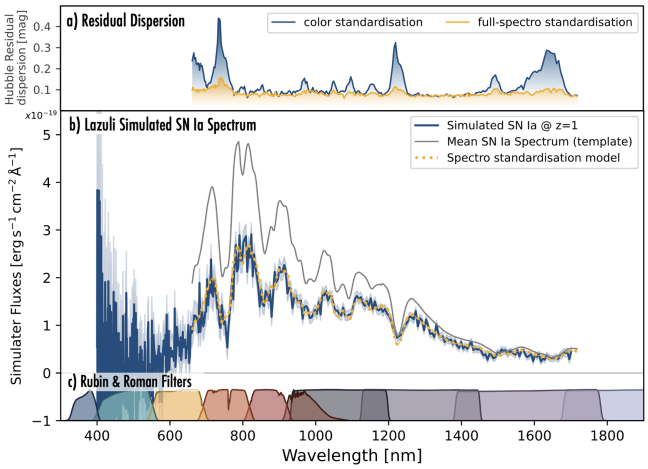

Figure 14. Simulated $z = 1$ SN Ia spectrum, as observed with the Lazuli IFS in 50 minutes (panel (b), in blue), made using `slicersim` (Rigault et al. 2026). The mean model spectrum is shown in gray, offset above, while the spectroscopic standardization prediction specific to this SN is shown in orange. The amplitude of this model orange line is not a free parameter but is derived from the SN spectroscopic behavior (K. Boone et al. 2021b,a). Above (panel (a)) is shown the SN Ia residual brightness scatter for an entire sample after applying the full "color+three intrinsic terms" spectroscopic standardization (orange), or if just using the dustlike color term (blue). This illustrates that the dustlike color term already achieves impressive standardization between SN Ia absorption lines, which strongly vary ($\gtrsim$0.3 mag). Distinguishing these variability origins at every redshift is challenging when employing broadband filters, as illustrated in the bottom panel (c) for LSST and (SN-related) HLTDS Roman filters.

These observatories will find transients early enough and with sufficient type-discriminating information that the Lazuli IFS will be able to obtain measurements for a sample having a high purity for SNe Ia near maximum light. This enables the use of spectroscopically "twin" SNe Ia, a novel technique to standardize SNe Ia using spectroscopy. H. K. Fakhouri et al. (2015), K. Boone et al. (2021a, 2021b), and G. Stein et al. (2022) have demonstrated the removal of three-fourths of the standardized brightness variance using spectrophotometry compared to classical light curve fitting applied to the exact same high-quality data. In addition to the resulting 4× statistical boost for every single SN, there is a substantial reduction in residuals as a function of host-galaxy environment, such as the infamous "mass step" (K. Boone et al. 2021a; C. Ganot et al. 2026). As shown in H. K. Fakhouri et al. (2015), finding "twin" SNe Ia is not hard once the sample size reaches a few hundred, and the method of K. Boone et al. (2021a) provides a nonlinear 3D latent space that removes the technical need for discrete "twin" SN Ia. While the Roman HLTDS will obtain such data in the form of spectral time series using its slitless prism mode (e.g., D. Rubin et al. 2025a), the Lazuli IFS, due to its lower background, larger aperture, and focus on SNe Ia at maximum light, will obtain a substantially larger spectrophotometric sample covering a larger redshift range continuously.

Figure 14 illustrates the underpinnings of the spectroscopic standardization approach; given a generic SN Ia spectrum at maximum light, one can reproduce its spectral shape and luminosity given a dustlike color term and the three intrinsic

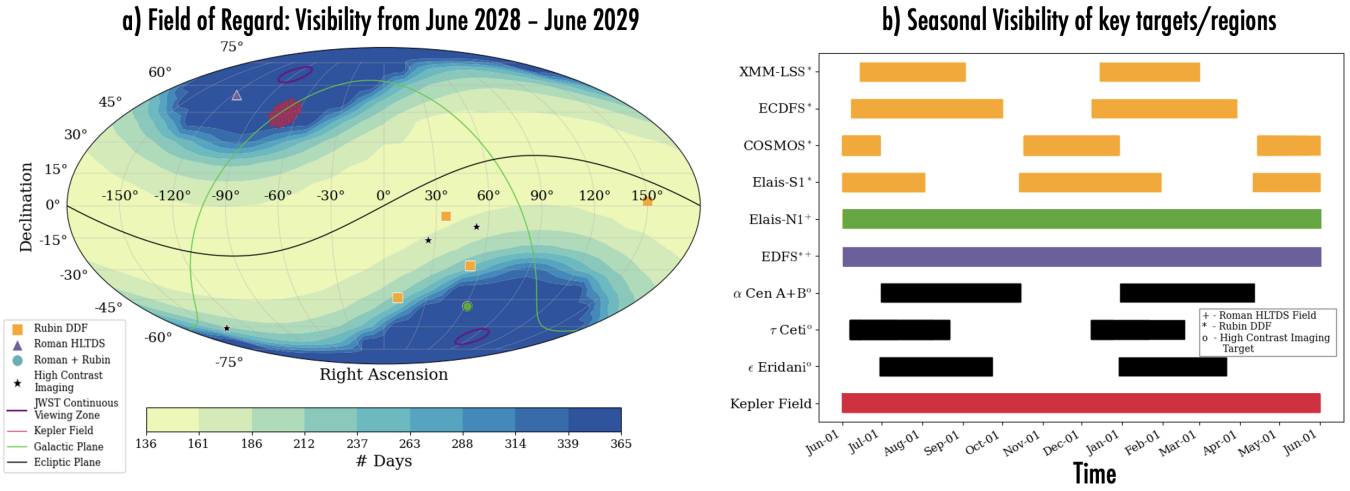

Figure 15. (a) Field of regard of the Lazuli Space Observatory, showing observability in days (color bar) across a year as a function of sky position. Key targets and/or fields of interest, including the Rubin DDFs (orange squares), Roman HLTDS field (purple triangle), and Roman/Rubin joint fields (green circle), Kepler field (red rectangles), example key high-contrast imaging targets (α Cen, τ Ceti, ϵ Eridani; black stars), and the JWST CVZs (purple circles), are highlighted. Additionally, the Galactic plane and Ecliptic plane are included as green and black lines, respectively. (b) For each of the key fields plotted in panel a, this panel shows their observability as a function of time throughout one year. Both panels use points sampled on a 10° grid over the sky to determine visibility.

parameters of the K. Boone et al. (2021a) nonlinear latent space. Figure 14(a) first illustrates the spectral variability after removing the dustlike color term (blue line), showing that regions associated with absorption lines have very large residual brightness scatter ($\geqslant$0.3 mag) while wavelengths in between have little scatter remaining. When next accounting for the terms of the 3D latent space (orange line in Figure 14(a)), all wavelengths become well-standardized, leading to a distance modulus scatter of $\sim$0.08 mag (K. Boone et al. 2021a); see also discussion in C. Ganot et al. (2026). Unlike spectroscopy, photometric standardization cannot disentangle these contributions since they cover wavelength ranges narrower than conventional filters. Additionally, stretch and color measured from light curves will be impacted differently as a function of redshift. While the Roman HLTDS will obtain SN Ia spectral time series using its slitless prism mode (e.g., D. Rubin et al. 2025a), the Lazuli IFS, due to its lower background, larger aperture, and focus on SNe Ia at maximum light, will obtain a substantially larger spectrophotometric sample covering a larger redshift range continuously.

The IFS observer-frame wavelength range from 400 to 1700 nm allows the observation of the rest-frame wavelength range of 400–680 nm for any target between $z = 0$ and $z = 1.5$, and the range of 400–850 nm up to $z = 1$. This uniquely enables SN Ia spectroscopic standardization based on a common rest-frame window with a single instrument from $z = 0$ to $z = 1.5$, as illustrated in Figure 14. As already demonstrated by the SEDmachine instrument (SEDm; N. Blagorodnova et al. 2018; M. Rigault et al. 2019; S. R. Kulkarni 2020), the Spectrograph for the Rapid Acquisition of Transients (SPRAT; A. S. Piascik et al. 2014), and the Folded Low Order whYte-pupil Double-dispersed Spectrograph(FLOYDS; T. M. Brown et al. 2013), the spectral resolution of $100 < R < 500$ employed by the Lazuli IFS is well suited for rapidly observing transient events like SNe, which have broad spectroscopic features due to their explosive nature.

Assuming expected performance, the Lazuli IFS will be able to achieve an average S/N of 20 per resolution element for rest-frame wavelengths of 400–680 nm for a typical $z = 1$ SN Ia spectrum in a 50 minute exposure, as illustrated in Figure 14. In comparison, a more nearby target with $z = 0.2$ would reach similar S/N levels in a couple of minutes, while a distant $z = 1.5$ target would require 4 hr. Increasing the target S/N to 30 per resolution element typically doubles the exposure time. Details concerning the Lazuli IFS exposure time calculator and spectral simulator—called `slicersim`—will be presented in M. Rigault et al. (2026).

Furthermore, such high-quality spectra will ensure spectroscopic redshifts for all SNe. In cases where there are spectroscopic redshifts for nearby galaxies, this information will aid in selecting the correct host galaxy. For cases with only photometric redshifts, the SN redshifts will reduce the statistical noise and potential systematic biases on the redshift axis of the expansion history measurement (e.g., M. Rigault et al. 2025).

Because the signal differentiating various cosmological models of interest is small, and since we wish to distinguish them with high confidence, measuring accurate SN Ia fluxes is paramount. Using an IFS rather than a slit spectrograph ensures that all of the SN light is collected, and that observations of the host galaxy after the SN has faded do not rely on expensive pointing accuracy or on a PSF that is stable over a period of years. Flux calibration of a ground-based IFS to the level afforded by the HST CALSPEC (e.g., R. C. Bohlin et al. 2020) system has been demonstrated (D. Rubin et al. 2022), as has the accurate subtraction of host galaxy background light (S. Bongard et al. 2011). By comparison, the Lazuli IFS will not need to deal with large variable image quality due to seeing, but diffraction effects, which vary linearly with wavelength, will be very important. SNe Ia at the highest redshifts are faint, requiring large collecting area, high throughput, and sufficient spectral and spatial resolution, as well as low detector noise, scattered light, and thermal background. The Lazuli IFS is expected to meet these demanding requirements. The parallel fields offer different spatial samplings at comparable spectral resolution, and the fields together cover enough area on the sky for accurate measurement of PSF wings, sampling of the sky, and host-galaxy subtraction. The need for a linear flux system over a range of $\mathcal{O}(10^4)$ in

brightness requires the very precise 2D and 3D calibration systems discussed in Section 4.5, so that the system can not only provide wavelength and flat-field calibration, but also monitor classical nonlinearity, count-rate nonlinearity, and problematic pixels in the detector.

S. Perlmutter et al. (in preparation) will provide more detail on a potential design for a powerful SN Ia-based study of dark energy behavior over cosmic time that the Lazuli IFS would be capable of conducting with spectrophotometry of $\mathcal{O}(10^4)$ SNe Ia. Rather than a two-parameter (w_0–w_a) fit, the goal would be $\sim$10 redshift bins of luminosity distance measurements out to $z \sim 1.5$. Lazuli spectroscopic follow-up of Roman, Rubin, and other targets from such a survey would also be made available to the community, enabling the (sub) classification of observed transients and determination of redshifts. Separate from the cosmological impact, having a large and uniform SN sample across a broad range of redshifts can yield key insights into the demographic evolution of SNe Ia and their progenitors or to train photometric classifiers (e.g., A. Möller & T. de Boissière 2020; H. Qu et al. 2021; U. F. Burhanudin & J. R. Maund 2023; K. M. de Soto et al. 2024; M. Vincenzi et al. 2024; R. C. Chen et al. 2026).

5.3.2. Cepheid Variables and the Hubble Constant

The Lazuli WCC will have several capabilities uniquely enabling it to contribute to the measurement of extragalactic distances using Cepheid variable stars. Cepheid variables are identified by their characteristic sawtooth-like temporal variations in brightness. In the optical, the amplitudes of these pulsations reach about a factor of 2 over a $\sim$10–100 day cycle. Twelve epochs of observation in at least one optical bandpass with a power-law sampling is a commonly used, optimal way to discover Cepheids (W. L. Freedman et al. 1994), used since the HST Key Project that resolved the factor of 2 debate over the value of the Hubble constant (W. L. Freedman et al. 2001). Indeed, the discovery of Cepheids beyond the Local Volume ($d \gtrsim 5$ Mpc) has for 30 years been the exclusive domain of HST, one which Lazuli is poised to join. Note that JWST's large slewing overheads and sharp drop in sensitivity blueward of 800 nm make the facility far too inefficient for the discovery of Cepheids, though it can still provide high-quality follow-up measurements in the NIR.

The Lazuli telescope will deliver diffraction-limited *r*-band images to the WCC, as well as be capable of fast slews, enabling the efficient discovery of individual Cepheid variables out to at least 40 Mpc. The adoption of Sloan Digital Sky Survey–like bandpasses will enable us to synergize with existing ground-based datasets such as Cepheids in M31 (M. Kodric et al. 2018, PAndromeda) and the upcoming LSST all-sky survey of the southern sky. LSST will provide extremely well-sampled observations of Cepheids in all southern targets out to 5 Mpc, providing a definitive calibration of the slope of the period–luminosity–metallicity (PLZ) relation, which continues to vary well outside of quoted uncertainties, as pointed out by D. Majaess (2024, 2025) and T. J. Hoyt et al. (2026).

Along with the improved ground-based synergies made possible by our choice of bandpasses, the telescope itself will provide significantly improved optical color measurements of known Cepheid variables in over 30 SN host galaxies, providing more accurate corrections for dust extinction as a result. The existing optical color measurements used by, e.g., A. G. Riess et al. (2022), for dust corrections are bottlenecked by low S/N, low-cadence observations. Lazuli would also discover new Cepheids in at least 15 more host galaxies that have hosted a SN suitable for cosmology, improving the precision of the calibration of the SN Ia luminosity. Finally, the flatter QE response of the qCMOS detectors in the WCC focal plane would enable tip of the red giant branch (TRGB) measurements in the *z*-band, which has been demonstrated to be an optimal filter like the *I* band for accurate TRGB measurements (M. Bellazzini & R. Pascale 2024). An upcoming paper (T. J. Hoyt et al. 2026, in preparation) will provide more details on a potential Hubble constant program based on Lazuli and the WCC.

5.3.3. Strong Gravitational Lensing

Strong gravitational lensing has long been recognized as a cosmological probe (S. Refsdal 1964), with systematic error sources largely decoupled from either SNe Ia standardized brightnesses or the lower rungs of the distance ladder used to infer the Hubble constant. The most common technique is the measurement of time delays between the different components of a strong lens. Due to their numbers and persistence, such measurements have historically used lensed active galactic nuclei (AGN) time delays (e.g., H0LICOW; K. C. Wong et al. 2020; TDCOSMO Collaboration et al. 2025), which vary over a wide range of timescales in a largely unpredictable manner. Thus, monitoring over the course of years is usually necessary, with specific strong but short-lived variations dominating the time-delay signal. More recently, monitoring of the transient sky has discovered strongly lensed SNe. Though much rarer than AGN, the advantage of SN lenses is twofold. First, the variation is comparatively strong and short-lived, offering greater precision for measuring time delays. Second, the SN eventually fades away, allowing the lensing galaxy to be better characterized. Correct measurement of the gravitational potential is the largest source of systematic uncertainty for the time-delay method, so ultimately this advantage is likely to become dominant. One aspect of this issue is the so-called "mass sheet degeneracy," which can be broken/reduced when the lensed sources have standardizable luminosities, as with SNe Ia. Lazuli spectrophotometry in particular will also offer a spectroscopic means for estimating time delays, and will help account for the effects of microlensing by stars within the lensing galaxy (see D. A. Goldstein et al. 2018; S. H. Suyu et al. 2024).

The advent of the Rubin, Roman, and LS4 surveys will lead to the discovery of hundreds of gravitationally lensed SNe (e.g., D. A. Goldstein et al. 2019). The Zwicky Transient Facility has already found several such lensed SNe; one recent example from the literature is the superluminous SN 2025wny (J. Johansson et al. 2025; S. Taubenberger et al. 2026) at $z \sim 2$ lensed by a pair of galaxies at $z \sim 0.4$. Another recent case that is still unfolding is SN 2025mkn (A. Goobar et al. 2025).

Follow-up of such new gravitationally lensed SNe will be vigorously pursued by both ground- and space-based facilities. Lazuli's field of regard (see Figure 15) will allow more temporally complete monitoring from space of both the key deep fields as well as the wider fields covered by the major

imaging surveys. Lazuli's WCC will be able to image these systems in the optical and NIR at spatial scales comparable to JWST.[15] The Lazuli IFS will be able to classify SN types, provide redshifts, provide better spectroscopic spatial resolution for lens modeling, and deliver spectrophotometric standardization of those that are SNe Ia. With these types of space-based follow-up, Lazuli will be able to make competitive measurements of the Hubble constant using time delays, as explored recently in, e.g., S. H. Suyu et al. (2024), E. E. Hayes et al. (2026).

Lazuli's IFS is also suited to disentangling strong lenses having multiple source planes. The geometry of the system constrains the source distances, while source spectroscopy determines redshifts. This provides a novel way to measure the expansion history of the Universe. Since lensed sources can have redshifts of several, this approach can also explore deep into the matter-dominated epoch. An especially beautiful example of such a system is the "Carousel Lens," with five source planes having been discovered so far (W. Sheu et al. 2024). For this case, the MUSE IFS proved especially valuable in identifying the different sources, and the Lazuli IFS can be similarly employed as new such systems are found. Its coverage to bluer wavelengths and with better spatial sampling than JWST, and higher Strehl ratio than ground-based AO at optical wavelengths, will be especially valuable for identifying Lyα emission systems.

6. Mission Operations

6.1. Orbit

Lazuli will operate in a 3:1 lunar-resonant HEO with perigee and apogee altitudes of approximately 70,000–285,000 km, a 9 day orbital period, and a 29° ecliptic inclination. The orbit is selected to maintain a stable resonance with the Moon, in which the spacecraft's orbital period is a simple integer fraction of the lunar orbital period, resulting in a repeatable long-term geometry. The orbit phasing is chosen such that close lunar perturbations are minimized over the mission lifetime, enabling predictable orbital evolution. This configuration provides a thermally stable environment, a low-radiation regime above Earth's trapped particle belts, minimal eclipses (approximately 2.4 hr per year), and continuous access to a large fraction of the sky. Near-continuous ground contact enables an average science data downlink of $\sim$70 GB day^{-1} and rapid response to targets of opportunity within hours of an external trigger.

Several operational orbits were evaluated for Lazuli, including inclined GEO, Sun-Earth L2, Earth-trailing heliocentric, and a range of MEOs. Trade studies examined radiation exposure, eclipse duration and frequency, Earth IR and albedo effects on instrument thermal stability, downlink data rates versus range, and maneuver complexity for final orbit insertion. These analyses led to the selection of a 3:1 lunar-resonant orbit, which provided optimal balance across mission-critical parameters.

The 3:1 resonance, flown previously by the IBEX mission (D. J. McComas et al. 2009), was selected over the 2:1 resonance flown by TESS because the lower apogee provides approximately 20% higher downlink capacity while maintaining equivalent sky coverage. Any point on the sky is observable for a minimum of 130 days per year, with continuous viewing zones (CVZs) at ecliptic latitudes $|\beta| \geqslant 54°$ (Figure 15). Full sky coverage is achieved within 106 days. The orbit is long-term stable, requiring minimal station-keeping maneuvers, maintaining perigee above the geosynchronous belt for at least 100 yr, and requiring no end-of-life disposal maneuvers.

Figure 15(a) shows the number of days that Lazuli will be able to view each point on the sky and several fields and targets of interest to potential science cases as described above in Section 5. Figure 15(b) shows the visibility of each of the fields marked in Figure 15(a) for a possible first year of Lazuli operations from 2028 June 1 to 2029 June 1. The Rubin DDFs are visible to Lazuli during their peak period of overhead visibility to Rubin from the ground. The Roman HLTDS fields are continuously visible to both Lazuli and Roman. Both figures are created using the Ansys/Systems Tool Kit (STK) Access and Coverage modules, integrated with custom Python code. As with TESS, there is a CVZ around the north and south celestial poles.

6.2. Operations Concept

Lazuli operations are designed around two principles: automation-first execution and rapid response to targets of opportunity. The ground segment will comprise a Science Operations Center (SOC) responsible for science planning, payload commanding, ToO validation, and data processing, and a Mission Operations Center (MOC) responsible for spacecraft bus operations, command uplink, and observatory state-of-health monitoring.

To fulfill a diverse range of science goals—from time-insensitive programs to tightly cadenced monitoring campaigns to disruptive targets of opportunity—all aspects of mission operations are being designed for flexibility and responsiveness. This includes: a dynamic queue scheduling system that can be recomputed on short timescales, balancing ToO interruptions against long-term scheduling efficiency and ongoing program completion; the capability for near-continuous commanding; and a strong emphasis on programmatic decision-making that evaluates both the scientific merit of incoming observations and the cost of disruption to the current schedule. The goal is to begin ToO observations within four hours of trigger receipt (for scientifically justified rapid-response ToOs) while maintaining high completion rates for cadenced and baseline programs.

The 4 hr threshold represents a mission requirement rather than a best-case or average figure. The total latency comprises ground-segment processing and schedule regeneration, command generation and uplink, and spacecraft slewing, settling, and target acquisition—the last of which dominates for large slew angles. Under favorable conditions, response times within the 90 minute goal should be achievable. A detailed treatment of the end-to-end ToO workflow and latency budget is presented in T. Wevers et al. (2026).

Central to this approach is the development of an intelligent dynamic queue intended to leverage recent advances in optimization algorithms and machine learning to assess the scientific impact of each observation, balance across multiple programs, and minimize duplication across observatories. The astronomical community has developed a diverse landscape of scheduling approaches—from mixed-integer programming solvers to dynamic figure-of-merit ranking—and Lazuli aims to integrate and build upon these methods. This includes

[15] Strehl ratios of 0.8 at 633 nm for Lazuli's unobscured 3 m versus 0.8 at 1100 nm for a segmented and obscured 6.5 m (Rigby et al. 2025).

exploring the potential use of large language model agents to augment scheduling decisions, an experimental approach consistent with Lazuli's philosophy of deploying front-line technology with the goal of testing and improving operations for future missions. This lean, automation-driven operations model draws on lessons from large space-based telescopes as well as rapid-response missions such as Swift (N. Gehrels et al. 2004), and queue-scheduled ground-based facilities including the Hobby–Eberly Telescope (M. Shetrone et al. 2007), NEID on the WIYN telescope (C. Schwab et al. 2016; H. Schweiker et al. 2024), ESO's Very Large Telescope (VLT; J. P. Anderson et al. 2024), and the "Keck Community Cadence" queue for the Keck Planet Finder (E. Petigura et al. 2022).

7. Community Access and Data Approach

The scientific impact of Lazuli will be measured by the excellence of research it enables across the global astronomical community. This section describes the guidelines governing community access to Lazuli observing time, data, and software. The Lazuli Space Observatory is part of the broader Eric and Wendy Schmidt Observatory System, which includes support for science operations, data archiving, and community access as integral parts of the space telescope program.

7.1. Community Engagement and Time Allocation Process

Engagement with the broader astronomical community is an integral part of the Lazuli mission. Community input is currently incorporated through a set of "science working groups" (SWGs) aligned with the observatory's primary capabilities: TDAMM SWG, stars and planets SWG, and cosmology SWG. Each working group includes external community members and has played a central role in shaping the observatory's core capabilities, including instrument requirements, observing modes, and performance priorities. As the mission matures and software tools, simulators, and documentation are released, scientists will gain an increasingly concrete understanding of Lazuli's capabilities and their relevance to specific research areas. In parallel, additional opportunities to contribute are expected to emerge, including engagement through SWGs and contributions to specialized areas such as software, scheduling, instrumentation, or observatory performance management.

Lazuli is envisioned as a community-access observatory, with observing time expected to be available to the global astronomical community through a merit-based, peer-reviewed time allocation committee (TAC) process. The allocation framework is intended to favor ambitious, collaborative programs that make full use of Lazuli's unique capabilities, including rapid response, broad wavelength coverage, and stable spectrophotometry, while still accommodating time-critical and disruptive opportunities. Details of the proposal process, allocation cadence, and operational implementation will be finalized as the observatory and its operations concept mature.

7.2. Data Access and Release

The default posture for Lazuli is open data release without extended proprietary periods. This approach is guided by best practices emerging across the astronomical community and by the scientific case for rapid, multifacility follow-up—goals that are impeded by extended embargoes, particularly for a mission with a years-long rather than decades-long operational lifetime.

A key consideration in developing data release guidelines is ensuring that open access does not disadvantage proposing teams. To this end, Lazuli is exploring mechanisms to reduce the overhead of proposing—including streamlined submission processes and planning tools—as well as structured support to help awarded investigators move quickly once data are in hand, such as science-ready pipelines, documentation, and analysis tools.

An integrated, cross-observatory Schmidt Observatory System data archive is considered foundational mission infrastructure. Desired features of such an archive include programmatic access via modern application programming interfaces (APIs), interoperability of data with other astronomical archives, reliable preservation, and—where feasible—co-located compute on a science platform to reduce barriers associated with large data transfers.

7.3. Software and Analysis Tools

Lazuli is conceived as a software-enabled observatory, in which scientific capability is defined not only by hardware performance but by the accessibility, transparency, and extensibility of its data systems. From mission inception, Lazuli's software ecosystem is being designed to support rapid scientific use, rigorous uncertainty propagation, and community participation.

All mission-developed scientific software—including data reduction pipelines, simulators, exposure time calculators, and archive interfaces—will be released under permissive open-source licenses and maintained in public repositories. This includes instrument-specific pipelines for the WCC, IFS, and ESC, as well as shared infrastructure for calibration handling, metadata validation, and provenance tracking.

The Lazuli pipelines follow a layered data model, progressing from raw, packetized telemetry to calibrated, science-ready products, while preserving intermediate data products and associated metadata to enable independent reprocessing and alternative analysis approaches. Standard community formats are adopted wherever possible (e.g., FITS for images and spectra, Parquet for large catalogs), and pipeline components are designed to be modular rather than monolithic, allowing individual stages to be reused, replaced, or bypassed as scientific needs evolve.

A defining feature of Lazuli's software strategy is the tight coupling between simulation, calibration, and analysis. High-fidelity instrument simulators—end-to-end diffraction simulators for the IFS and ESC—along with exposure time calculators, such as `slicersim` for the IFS and similar tools for the WCC, are developed alongside the pipelines and share common configuration files and assumptions.

This codevelopment enables forward-modeling approaches in which detector-level data can be fit directly, preserving photon statistics and correlated noise, while also providing fast "quick-look" reductions for rapid transient classification and follow-up.

Exposure time calculators and performance modeling tools are treated as first-class scientific products rather than ancillary utilities. These tools are version-controlled, scriptable, and designed to interface directly with evolving throughput budgets, calibration knowledge, and mission configuration

parameters, enabling reproducible trade studies and transparent assessment of observational feasibility.

Recognizing that software sustainability is essential for scientific impact, the Lazuli project commits to maintaining core analysis tools throughout the mission lifetime, with continuous integration testing, public documentation, and example workflows. Where appropriate, Lazuli will align with and contribute to existing community software ecosystems rather than duplicating effort.

Finally, Lazuli's software and data systems are explicitly designed to support open science. Data products, pipelines, and simulators are intended to be usable not only by proposing teams but by the broader community immediately upon release, lowering barriers to entry and enabling independent validation, method development, and cross-observatory analyses. In this sense, Lazuli aims not only to deliver data, but to provide a shared computational framework within which new science questions can be posed and answered.

8. Conclusion

The Lazuli Space Observatory is designed to address a well-defined gap in the current and near-future astrophysical landscape: the absence of a large-aperture, space-based optical–NIR facility capable of rapid response, stable spectrophotometry, and broad wavelength coverage. By combining a 3 m aperture telescope with a focused instrument suite and an operations concept optimized for flexibility, Lazuli enables observations that are difficult or impossible with existing or planned facilities, particularly for fast-evolving and time-critical phenomena.

Lazuli's capabilities support a broad range of science, spanning TDAMM, exoplanet characterization, and precision cosmology. Its ability to obtain continuous 400–1700 nm spectrophotometry, multiband optical imaging, and high-contrast coronagraphic observations from a single platform enables new approaches to transient classification, early-time physical inference, and spectrophotometric standardization. Equally important, the mission is designed to operate in coordination with contemporaneous facilities—including wide-field time-domain surveys, gravitational-wave detectors, and UV, X-ray, and IR space observatories—maximizing scientific return through complementary observations.

Beyond its immediate scientific reach, Lazuli serves as a testbed for an alternative model of space observatory development. The mission demonstrates how constrained cost, accelerated schedules, and deliberate risk acceptance can be used to deploy ambitious capabilities while scientific questions remain timely. In this sense, Lazuli functions both as a general-purpose astrophysics facility and as a pathfinder for future missions that prioritize responsiveness, software-enabled operations, and community accessibility.

The capabilities described in this paper represent design requirements and modeled expectations; realizing them fully requires navigating several open challenges. The compressed development timeline, while deliberate, implies a demanding assembly, integration, and test schedule and a commissioning period in which all three instruments must be verified to meet their design specifications in orbit. Ground-segment development—including data systems, pipeline infrastructure, and community-facing software tools—has necessarily been prioritized behind the space segment and will require sustained effort through launch and into operations. The rapid-response scheduling system, while informed by analysis and heritage from prior missions, has not yet been demonstrated at the system level. These challenges are being actively managed through a program of independent technical reviews and by incorporating best practices from the broader space telescope community, consistent with the mission's philosophy of deliberate risk acceptance in service of accelerated scientific return.

Together, these elements position Lazuli to deliver high-impact science in the late 2020s while informing the design, operation, and scientific use of the next generation of space-based observatories.

Acknowledgments

This work was supported by Schmidt Sciences. We acknowledge SEE and Quartus for key engineering studies for Lazuli. M.R. acknowledges Y. Copin, M. Aubert, and C. Ganot for scientific feedback. Time-domain research by D. J.S. is supported by NSF grants 2108032, 2308181, 2407566, and 2432036, as well as by the Heising–Simons Foundation under grant 20201864. We thank Hiram Olivas and Grant West for their contributions, including the CAD rendering of the ESC in Figure 6.

Author Contributions

A.R. serves as Mission Scientist and Head of the Science Mission Office for Lazuli. S.F., P.K., S.P., E.S.D., and S.P.W. contribute to mission leadership. J.D., F.Y.Y., and S.R.Z. contribute to systems engineering and observatory implementation. T.W., N.A., and J.L. serve as science working group leads. A.R., S.P., T.W., N.A., J.L., G.A., M.R., T.J.H., P.G., E.S.D., G.F., P.I., D.K., R.A., J.H., J.E., L.L., G.S., E.S., I.J.M. C., J.P., C.S., A.P., S.G., D.J.S., T.N.M., M.A.A.Z., A.S., L.P., K.K., H.C., K.D., M.E., H.K., D.K., J.R.M., T.J.M., K.M., K.L.M., P.N., S.R., S.S., I.I.S., S.K.S., K.V.G., A.F.W., J.Y., H.K., and others contribute to science capability definition, instrumentation, optical design, software, data systems, and survey development. All authors contributed to mission development and reviewed the manuscript.

ORCID iDs

Arpita Roy https://orcid.org/0000-0001-8127-5775
Stuart Feldman https://orcid.org/0000-0003-0963-3640
Saul Perlmutter https://orcid.org/0000-0002-4436-4661
Ewan S. Douglas https://orcid.org/0000-0002-0813-4308
Gabor Furesz https://orcid.org/0000-0001-8467-9767
Patrick Ingraham https://orcid.org/0000-0003-3715-8138
Gudmundur Stefansson https://orcid.org/0000-0001-7409-5688
Thomas Wevers https://orcid.org/0000-0002-4043-9400
Nicole Arulanantham https://orcid.org/0000-0003-2631-5265
James Lasker https://orcid.org/0000-0003-2999-4873
Mickael Rigault https://orcid.org/0000-0002-8121-2560
Everett Schlawin https://orcid.org/0000-0001-8291-6490
Sander R. Zandbergen https://orcid.org/0000-0002-3548-4696
S. Pete Worden https://orcid.org/0000-0001-8834-9108
Ramya Anche https://orcid.org/0000-0002-4989-6253
Jerry Edelstein https://orcid.org/0009-0002-2419-8819
Suvi Gezari https://orcid.org/0000-0003-3703-5154

Justin Hom https://orcid.org/0000-0001-9994-2142
Taylor J. Hoyt https://orcid.org/0000-0001-9664-0560
Hyukmo Kang https://orcid.org/0000-0002-2224-1353
Daewook Kim https://orcid.org/0000-0002-1122-8727
Keerthi Kunnumkai https://orcid.org/0009-0000-4830-1484
Leander Lacroix https://orcid.org/0000-0003-0629-5746
Jared R. Males https://orcid.org/0000-0002-2346-3441
Kian Milani https://orcid.org/0000-0001-9204-2299
Timothy N Miller https://orcid.org/0009-0005-2445-7544
Antonella Palmese https://orcid.org/0000-0002-6011-0530
Jason Pero https://orcid.org/0009-0000-2075-1109
Laurent Pueyo https://orcid.org/0000-0003-3818-408X
David J. Sand https://orcid.org/0000-0003-4102-380X
Christian Schneider https://orcid.org/0000-0002-5094-2245
Sanchit Sabhlok https://orcid.org/0000-0002-8780-8226
Arfon Smith https://orcid.org/0000-0002-3957-2474
Kyle Van Gorkom https://orcid.org/0000-0002-4877-7762
Andre F. Wong https://orcid.org/0009-0008-2893-774X
Jaegun Yoo https://orcid.org/0009-0002-0291-4933
Md Abdullah Al Zaman https://orcid.org/0000-0002-3696-2127

References

Abbott, B. P., Abbott, R., Abbott, T.D., et al. 2017, ApJL, 848, L12
Adame, A. G., Aguilar, J., Ahlen, S., et al. 2025, JCAP, 2025, 021
Akeson, R., Armus, L., Bachelet, E., et al. 2019, arXiv:1902.05569
Alarcón, F., Bergin, E. A., & Cugno, G. 2024, ApJ, 966, 225
Aldering, G., Akerlof, C. W., Amanullah, R., et al. 2002, SPIE, 4835, 146
Amara, A., & Quanz, S. P. 2012, MNRAS, 427, 948
Anan, T., Jaeggli, S., Lin, H., et al. 2024, SPIE, 13096, 1309626
Anderson, J. P., Sedaghati, E., Cikota, A., et al. 2024, SPIE, 13098, 1309805
Andreoni, I., Ackley, K., Cooke, J., et al. 2017, PASA, 34, e069
Andrews, S. M., Huang, J., Pérez, L. M., et al. 2018, ApJL, 869, L41
Andrews, S. M., Wilner, D. J., Espaillat, C., et al. 2011, ApJ, 732, 42
Aoyama, Y., Ikoma, M., & Tanigawa, T. 2018, ApJ, 866, 84
Arcavi, I. 2018, ApJL, 855, L23
Arcavi, I., Hosseinzadeh, G., Howell, D. A., et al. 2017, Natur, 551, 64
Ashcraft, J. N., Choi, H., Douglas, E. S., et al. 2022, SPIE, 12180, 121805L
Ashcraft, J. N., Douglas, E. S., Anche, R. M., et al. 2024, SPIE, 13092, 130926K
Atreya, S. K., Crida, A., Guillot, T., et al. 2022, arXiv:2205.06914
Avenhaus, H., Quanz, S. P., Garufi, A., et al. 2018, ApJ, 863, 44
Bailey, V. P., Bendek, E., Monacelli, B., et al. 2023, SPIE, 12680, 126800T
Batalha, N. E., Marley, M. S., Lewis, N. K., & Fortney, J. J. 2019, ApJ, 878, 70
Batalha, N. E., Smith, A. J. R. W., Lewis, N. K., et al. 2018, AJ, 156, 158
Baudoz, P., Boccaletti, A., Baudrand, J., & Rouan, D. 2005, IAUS, 1, 553
Bellazzini, M., & Pascale, R. 2024, A&A, 691, A42
Bianco, F. B., Ivezić, Ž., Jones, R. L., et al. 2022, ApJS, 258, 1
Bifano, T. G., Mali, R. K., Dorton, J. K., et al. 1997, OptEn, 36, 1354
Blagorodnova, N., Neill, J. D., Walters, R., et al. 2018, PASP, 130, 035003
Bohlin, R. C., Hubeny, I., & Rauch, T. 2020, AJ, 160, 21
Bongard, S., Soulez, F., Thiébaut, É., & Pecontal, É. 2011, MNRAS, 418, 258
Bonse, M. J., Gebhard, T. D., Dannert, F. A., et al. 2025, AJ, 169, 194
Boone, K., Aldering, G., Antilogus, P., et al. 2021a, ApJ, 912, 71
Boone, K., Aldering, G., Antilogus, P., et al. 2021b, ApJ, 912, 70
Borucki, W. J., Koch, D., Basri, G., et al. 2010, Sci, 327, 977
Boss, A. P. 2025, ApJ, 982, 17
Bowler, B. P. 2016, PASP, 128, 102001
Brout, D., Scolnic, D., Popovic, B., et al. 2022, ApJ, 938, 110
Brown, T. M., Baliber, N., Bianco, F. B., et al. 2013, PASP, 125, 1031
Bruna, M., Cowan, N. B., Sheffler, J., et al. 2023, MNRAS, 519, 460
Bryson, S., Kunimoto, M., Belikov, R., et al. 2025, PASP, 137, 124401
Burhanudin, U. F., & Maund, J. R. 2023, MNRAS, 521, 1601
Cady, E., Bowman, N., Greenbaum, A. Z., et al. 2025, JATIS, 11, 021408
Castelli, F., & Kurucz, R. L. 2003, in 210th Symposium of the IAU, ed. N. Piskunov, W.W. Weiss, & D.F. Gray
Changeat, Q., Lagage, P.-O., Tinetti, G., et al. 2025, arXiv:2509.02657
Chauvin, G. 2024, CRPhy, 24, 139
Chen, C., & Shen, R.-F. 2025, ApJ, 991, 180
Chen, R. C., Guo, Z., Scolnic, D., et al. 2026, ApJ, 999, 81
Chornock, R., Berger, E., Kasen, D., et al. 2017, ApJL, 848, L19
Close, L. M., Males, J. R., Li, J., et al. 2025b, AJ, 169, 35
Close, L. M., van Capelleveen, R. F., Weible, G., et al. 2025a, ApJL, 990, L9
Cook, T., Cahoy, K., Chakrabarti, S., et al. 2015, JATIS, 1, 044001
Cowperthwaite, P. S., Berger, E., Villar, V. A., et al. 2017, ApJL, 848, L17
Crilly, A., Malivert, A., Jørgensen, A. C. S., et al. 2025, PLSCB, 21, e1013259
Cugno, G., Facchini, S., Alarcon, F., et al. 2025, AJ, 170, 317
de Soto, K. M., Villar, V. A., Berger, E., et al. 2024, ApJ, 974, 169
Derby, K., Milani, K., Hathaway, G. C., et al. 2025, SPIE, 13627, 644
Derby, K. Z., Milani, K., Blomquist, S., et al. 2023, SPIE, 12677, 126770I
DES Collaboration, Abbott, T.M.C., Acevedo, M., et al. 2024, ApJL, 973, L14
DESI Collaboration, Abdul Karim, M., Aguilar, J., et al. 2025, PhRvD, 112, 083515
Douglas, E., Allan, G., Morgan, R., et al. 2021, FRASS, 8, 676281
Douglas, E. S., Aldering, G., Allan, G. W., et al. 2023, SPIE, 12677, 126770D
Douglas, E. S., Debes, J., Mennesson, B., et al. 2022, PASP, 134, 024402
Douglas, E. S., Mendillo, C. B., Cook, T. A., Cahoy, K. L., & Chakrabarti, S. 2018, JATIS, 4, 019003
Drout, M. R., Piro, A. L., Shappee, B. J., et al. 2017, Sci, 358, 1570
Ealet, A., Prieto, E., Bonissent, A., et al. 2006, SPIE, 6265, 626533
Ertel, S., Pearce, T. D., Debes, J. H., et al. 2025, PASP, 137, 031001
Esposito, T. M., Kalas, P., Fitzgerald, M. P., et al. 2020, AJ, 160, 24
Evans, P. A., Cenko, S. B., Kennea, J. A., et al. 2017, Sci, 358, 1565
Fakhouri, H. K., Boone, K., Aldering, G., et al. 2015, ApJ, 815, 58
Feinstein, A. D., Radica, M., Welbanks, L., et al. 2023, Natur, 614, 670
Fernandes, R. B., Johnson, S., Bergsten, G. J., et al. 2025, PASP, 137, 121001
Fitzgerald, M. P., Sallum, S., Millar-Blanchaer, M., et al. 2022, SPIE, 12184, 1218426
Follette, K. B., Close, L. M., Males, J. R., et al. 2023, AJ, 165, 225
Freedman, W. L., Hughes, S. M., Madore, B. F., et al. 1994, ApJ, 427, 628
Freedman, W. L., Madore, B. F., Gibson, B. K., et al. 2001, ApJ, 553, 47
Ganot, C., Copin, Y., Rigault, M., et al. 2026, A&A, 710, A315
Gao, G., Pasquale, B. A., Marx, C. T., & Chambers, V. J. 2017, Optical Design and Fabrication 2017 (Freeform, IODC, OFT) (Optica Publishing Group), ITh1B.3, doi:10.1364/IODC.2017.ITh1B.3
Gardner, J. P., Mather, J. C., Clampin, M., et al. 2006, SSRv, 123, 485
Garufi, A., Benisty, M., Pinilla, P., et al. 2018, A&A, 620, A94
Gehrels, N., Chincarini, G., Giommi, P., et al. 2004, ApJ, 611, 1005
Gilliland, R. L., Chaplin, W. J., Dunham, E. W., et al. 2011, ApJS, 197, 6
Give'on, A., Kern, B., Shaklan, S., Moody, D. C., & Pueyo, L. 2007, SPIE, 6691, 66910A
Goldstein, D. A., Nugent, P. E., & Goobar, A. 2019, ApJS, 243, 6
Goldstein, D. A., Nugent, P. E., Kasen, D. N., & Collett, T. E. 2018, ApJ, 855, 22
Goobar, A., Lemon, C., Johansson, J., et al. 2025, TNSAN, 201, 1
Guerrero, N. M., Seager, S., Huang, C. X., et al. 2021, ApJS, 254, 39
Guimond, C. M., & Cowan, N. B. 2019, AJ, 157, 188
Guyon, O. 2018, ARA&A, 56, 315
Guyon, O., Sevin, A., Gratadour, D., et al. 2018, SPIE, 10703, 107031E
Haffert, S. Y., Bohn, A. J., de Boer, J., et al. 2019, NatAs, 3, 749
Haffert, S. Y., Males, J. R., Ahn, K., et al. 2023, A&A, 673, A28
Hallinan, G., Ravi, V., Weinreb, S., et al. 2019, BAAS, 51, 255
Hayes, E. E., Dhawan, S., Thorp, S., Pierel, J. D. R., & Arendse, N. 2026, MNRAS, 546, stag113
Ho, A. Y. Q., Perley, D. A., Chen, P., et al. 2023, Natur, 623, 927
Holler, B. J., Milam, S. N., Bauer, J. M., et al. 2018, JATIS, 4, 034003
Holman, M. J., & Murray, N. W. 2005, Sci, 307, 1288
Howell, S. B., Sobeck, C., Haas, M., et al. 2014, PASP, 126, 398
Hoyt, T. J., Jang, I. S., Freedman, W. L., et al. 2026, ApJ, 1002, 11
Hubble, E. 1929, PNAS, 15, 168
Huie, R., Mears, A., Montoya, M., et al. 2024, SPIE, 13134, 131340M
Ivezić, Ž., Kahn, S. M., Tyson, J. A., et al. 2019, ApJ, 873, 111
Jenkins, J. M., Twicken, J. D., McCauliff, S., et al. 2016, SPIE, 9913, 99133E
Jensen-Clem, R., Hinz, P. M., van Kooten, M. A. M., et al. 2022, SPIE, 12185, 1218546
Johansson, J., Perley, D. A., Goobar, A., et al. 2025, ApJL, 995, L17
Kane, S. R. 2025, AJ, 170, 329
Kasdin, N. J., Bailey, V. P., Mennesson, B., et al. 2020, SPIE, 11443, 114431U
Kasen, D., Metzger, B., Barnes, J., Quataert, E., & Ramirez-Ruiz, E. 2017, Natur, 551, 80
Kasliwal, M. M., Nakar, E., Singer, L. P., et al. 2017, Sci, 358, 1559
Keppler, M., Benisty, M., Müller, A., et al. 2018, A&A, 617, A44

Kim, D., Choi, H., Brendel, T., et al. 2021, OEA, 4, 210040
Kipping, D. M. 2009, MNRAS, 396, 1797
Ko, C.-L., Douglas, E. S., & Hom, J. 2024, SPIE, 13138, 1313811
Kodric, M., Riffeser, A., Hopp, U., et al. 2018, AJ, 156, 130
Kreidberg, L., Bean, J. L., Désert, J.-M., et al. 2014, ApJL, 793, L27
Krishnanth, P. M. S., Douglas, E. S., Anche, R. M., et al. 2024, AJ, 168, 169
Krist, J., Effinger, R., Kern, B., et al. 2018, SPIE, 10698, 106982K
Kulkarni, S. R. 2020, arXiv:2004.03511
Kulkarni, S. R., Harrison, F. A., Grefenstette, B. W., et al. 2021, arXiv:2111.15608
Kunimoto, M., & Matthews, J. M. 2020, AJ, 159, 248
Kunnumkai, K., Palmese, A., Bulla, M., et al. 2025a, PhRvD, 112, 123005
Kunnumkai, K., Palmese, A., Farah, A. M., et al. 2025b, ApJ, 993, 15
Law, N. M., Corbett, H., Galliher, N. W., et al. 2022, PASP, 134, 035003
Leavitt, H. S., & Pickering, E. C. 1912, HarCi, 173, 1
Limbach, M. A., Lustig-Yaeger, J., Vanderburg, A., et al. 2024, AJ, 168, 57
Long, F., Herczeg, G. J., Harsono, D., et al. 2019, ApJ, 882, 49
Long, F., Pinilla, P., Herczeg, G. J., et al. 2018, ApJ, 869, 17
Long, J. D., Males, J. R., Close, L. M., et al. 2024, SPIE, 13097, 130972X
Lupu, R. E., Marley, M. S., Lewis, N., et al. 2016, AJ, 152, 217
Maier, E. R., Douglas, E. S., Kim, D. W., et al. 2020, SPIE, 11443, 114431Y
Majaess, D. 2024, MNRAS, 529, 2627
Majaess, D. 2025, AstBu, 80, 545
Males, J. R., Close, L. M., Haffert, S. Y., et al. 2024a, SPIE, 13097, 1309709
Males, J. R., Close, L. M., Haffert, S. Y., et al. 2024b, SPIE, 13096, 130960Y
Margutti, R., Metzger, B. D., Chornock, R., et al. 2019, ApJ, 872, 18
Mawet, D., Serabyn, E., Liewer, K., et al. 2010, ApJ, 709, 53
Mazoyer, J., & Pueyo, L. 2017, SPIE, 10400, 1040014
McComas, D. J., Allegrini, F., Bochsler, P., et al. 2009, SSRv, 146, 11
Mendillo, C. B., Ashcraft, J. N., Derby, K. Z., et al. 2023a, SPIE, 12680, 126802E
Mendillo, C. B., Chakrabarti, S., Cook, T. A., Hicks, B. A., & Lane, B. F. 2012, ApOpt, 51, 7069
Mendillo, C. B., Hewawasam, K., Howe, G., et al. 2020, AAS, 235, 320.02
Mendillo, C. B., Hewawasam, K., Martel, J., et al. 2023b, JATIS, 9, 025005
Mendillo, C. B., Howe, G. A., Hewawasam, K., et al. 2017, SPIE, 10400, 1040010
Mennesson, B., Belikov, R., Por, E., et al. 2024, JATIS, 10, 035004
Metzger, B. D. 2020, LRR, 23, 1
Metzger, B. D., & Perley, D. A. 2023, ApJ, 944, 74
Meyers, J., Kirkby, D., & Thomas, D. 2019, batoid, Version 0.1, DOE CODE,
Milani, K., Douglas, E., Haffert, S., & Van Gorkom, K. 2023, SPIE, 12680, 126800Z
Milani, K., Douglas, E. S., Haffert, S. Y., & Gorkom, K. V. 2024, JATIS, 10, 029001
Milani, K., Van Gorkom, K., Mendillo, C. B., et al. 2025b, SPIE, 13627, 623
Milani, K., Will, S. D., Gorkom, K. J. V., et al. 2025a, JATIS, 11, 039001
Miller, A. A., Abrams, N. S., Aldering, G., et al. 2025, PASP, 137, 094204
Miller, K., & Guyon, O. 2016, SPIE, 9909, 99094G
Miller, K., Guyon, O., & Males, J. 2017, JATIS, 3, 049002
Möller, A., & de Boissière, T. 2020, MNRAS, 491, 4277
Morgan, R. E., Douglas, E. S., Allan, G., et al. 2021, JATIS, 7, 024002
Nakar, E., & Piran, T. 2017, ApJ, 834, 28
National Academies of Sciences, Engineering, and Medicine 2021, Pathways to Discovery in Astronomy and Astrophysics for the 2020s (The National Academies Press)
N'Diaye, M., Choquet, E., Pueyo, L., et al. 2013, SPIE, 8864, 88641K
Nemati, B., Krist, J., Poberezhskiy, I., & Kern, B. 2023, JATIS, 9, 034007
Nemati, B., Krist, J. E., & Mennesson, B. 2017, SPIE, 10400, 1040007
Nutzman, P. A., Fabrycky, D. C., & Fortney, J. J. 2011, ApJL, 740, L10
Okuta, R., Unno, Y., Nishino, D., Hido, S., & Loomis, C. 2017, in 31st Conf. on Neural Information Processing System
Page, C. L., D'Cruz, C., Redmond, S. F., et al. 2025, SPIE, 13606, 136060L
Pasquale, B. A., Peretz, E., Gao, G., et al. 2024, SPIE, 13096, 1309660
Patra, K. C., Winn, J. N., Holman, M. J., et al. 2017, AJ, 154, 4
Penny, M. T., Gaudi, B. S., Kerins, E., et al. 2019, ApJS, 241, 3
Perley, D. A., Mazzali, P. A., Yan, L., et al. 2019, MNRAS, 484, 1031
Perlmutter, S., Aldering, G., Goldhaber, G., & Project, T. S. C. 1999, ApJ, 517, 565
Petigura, E., Howard, A., Isaacson, H., et al. 2022, arXiv:2207.06523
Phillips, M. M. 1993, ApJL, 413, L105
Pian, E., D'Avanzo, P., Benetti, S., et al. 2017, Natur, 551, 67
Piascik, A. S., Steele, I. A., Bates, S. D., et al. 2014, SPIE, 9147, 91478H
Planck Collaboration, Aghanim, N., Akrami, Y., et al. 2020, A&A, 641, A6
Plunkett, C., Follette, K. B., Marleau, G.-D., & Nielsen, E. L. 2025, AJ, 169, 262
Pogorelyuk, L., Fitzgerald, R., Vlahakis, S., Morgan, R., & Cahoy, K. 2022, ApJ, 937, 66
Poleski, R., Skowron, J., Mróz, P., et al. 2021, AcA, 71, 1
Potier, A., Baudoz, P., Galicher, R., Singh, G., & Boccaletti, A. 2020, A&A, 635, A192
Potier, A., Prada, C. M., Ruane, G., et al. 2023, JATIS, 9, 029001
Prentice, S. J., Maguire, K., Smartt, S. J., et al. 2018, ApJL, 865, L3
Pueyo, L. 2018, in Handbook of Exoplanets, ed. H. J. Deeg & J. A. Belmonte (Springer), 1, doi:10.1007/978-3-319-30648-3_10-1
Qu, H., Sako, M., Möller, A., & Doux, C. 2021, AJ, 162, 67
Quanz, S. P., Ottiger, M., Fontanet, E., et al. 2022, A&A, 664, A21
Rackham, B. V., Apai, D., & Giampapa, M. S. 2019, AJ, 157, 96
Rao, R. 2024, Natur, 626, 464
Rauer, H., Catala, C., Aerts, C., et al. 2014, ExA, 38, 249
Refsdal, S. 1964, MNRAS, 128, 307
Ren, B., Pueyo, L., Zhu, G. B., Debes, J., & Duchêne, G. 2018, ApJ, 852, 104
Reynolds, C. S., Kara, E. A., Mushotzky, R. F., et al. 2023, SPIE, 12678, 126781E
Ricker, G. R., Winn, J. N., Vanderspek, R., et al. 2015, JATIS, 1, 014003
Riess, A. G., & Breuval, L. 2024, in At the crossroads of astrophysics and cosmology: Period-luminosity relations in the 2020s, Vol. 376, ed. R, de Grijs, P. A. Whitelock, & M. Catelan (Cambridge Univ. Press), 15
Riess, A. G., Filippenko, A. V., Challis, P., et al. 1998, AJ, 116, 1009
Riess, A. G., Press, W. H., & Kirshner, R. P. 1996, ApJ, 473, 88
Riess, A. G., Yuan, W., Macri, L. M., et al. 2022, ApJL, 934, L7
Rigault, M., Copin, Y., Aldering, G., et al. 2026, arXiv:2607.06391
Rigault, M., Neill, J. D., Blagorodnova, N., et al. 2019, A&A, 627, A115
Rigault, M., Smith, M., Goobar, A., et al. 2025, A&A, 694, A1
Rizk, B., Drouet d'Aubigny, C., Golish, D., et al. 2018, Space Sci Rev, 214, 26
Roberge, A., Chen, C. H., Millan-Gabet, R., et al. 2012, PASP, 124, 799
Roman, N. G. 1974, Large Space Telescope—A New Tool for Science, 12, 11
Roman Observations Time Allocation CommitteeCore Community Survey Definition Committees 2025, arXiv:2505.10574
Ruane, G., Mawet, D., Jewell, J., & Shaklan, S. 2017, SPIE, 10400, 104000J
Ruane, G., Mawet, D., Mennesson, B., Jewell, J. B., & Shaklan, S. B. 2018, JATIS, 4, 015004
Ruane, G., Riggs, A. J. E., Serabyn, E., et al. 2022, SPIE, 12180, 1218024
Rubin, D., Aldering, G., & Fruchter, A. 2025a, arXiv:2506.04327
Rubin, D., Aldering, G., Antilogus, P., et al. 2022, ApJS, 263, 1
Rubin, D., Aldering, G., Betoule, M., et al. 2025b, ApJ, 986, 231
Rubin's Survey Cadence Optimization Committee, Bianco, F. B., Jones, R. L., Anguita, T., et al. 2025, PSTN-056: Survey Cadence Optimization Committee's Phase 3 Recommendations, NSF-DOE Vera C. Rubin Observatory Technical Report, 10.71929/RUBIN/2585402
Rustamkulov, Z., Sing, D. K., Mukherjee, S., et al. 2023, Natur, 614, 659
Sanchis-Ojeda, R., & Winn, J. N. 2011, ApJ, 743, 61
Savransky, D., Delacroix, C., & Garrett, D. 2017, ascl soft, ascl:1706.010
Schwab, C., Rakich, A., Gong, Q., et al. 2016, SPIE, 9908, 99087H
Schweiker, H., Logsdon, S. E., Everett, M., et al. 2024, SPIE, 13098, 1309808
Serabyn, G., Mawet, D., Ruane, G., Mejia-Prada, C., & Jovanovic, N. 2019, TECHNOLOGY DEVELOPMENT FOR EXOPLANET MISSONS: Technology Milestone White Paper Vortex Coronagraph Technology, TDEM White Paper, JPL TDEM Whitepaper, https://exoplanets.nasa.gov/internal_resources/1366/
Shetrone, M., Cornell, M. E., Fowler, J. R., et al. 2007, PASP, 119, 556
Sheu, W., Cikota, A., Huang, X., et al. 2024, ApJ, 973, 3
Shvartzvald, Y., Waxman, E., Gal-Yam, A., et al. 2024, ApJ, 964, 74
Singh, G., Lozi, J., Guyon, O., et al. 2015, PASP, 127, 857
Skaf, N., Jensen-Clem, R., Hunter, A., et al. 2024, arXiv:2409.13126
Smartt, S. J., Chen, T.-W., Jerkstrand, A., et al. 2017, Natur, 551, 75
Soares-Santos, M., Holz, D. E., Annis, J., et al. 2017, ApJL, 848, L16
Soummer, R., Pueyo, L., & Larkin, J. 2012, ApJ, 755, L28
Space Telescope Science Institute 2024, Hubble Space Telescope Status, https://hubblesite.org/mission-and-telescope/hubble-status
Spergel, D., Gehrels, N., Baltay, C., et al. 2015, arXiv:1503.03757
Stark, C. C., Mennesson, B., Bryson, S. T., et al. 2024, JATIS, 10, 034006
Stein, G., Seljak, U., Böhm, V. & Nearby Supernova Factory 2022, ApJ, 935, 5
STScI Development Team 2013, ascl soft, ascl:1303.023
Stumpe, M. C., Smith, J. C., Van Cleve, J. E., et al. 2012, PASP, 124, 985
Sun, Q., Wang, S. X., Welbanks, L., Teske, J., & Buchner, J. 2024, AJ, 167, 167
Suyu, S. H., Goobar, A., Collett, T., More, A., & Vernardos, G. 2024, SSRv, 220, 13
Tanvir, N. R., Levan, A. J., González-Fernández, C., et al. 2017, ApJL, 848, L27

Taubenberger, S., Acebron, A., Cañameras, R., et al. 2026, A&A, 710, A365
TDCOSMO Collaboration, Birrer, S., Buckley-Geer, E.J., et al. 2025, A&A, 704, A63
Teachey, A., & Kipping, D. M. 2018, SciA, 4, eaav1784
Trauger, J. T., & Traub, W. A. 2007, Natur, 446, 771
Tripp, R. 1998, A&A, 331, 815
Troja, E., Piro, L., van Eerten, H., et al. 2017, Natur, 551, 71
Uddin, S. A., Burns, C. R., Phillips, M. M., et al. 2024, ApJ, 970, 72
Utsumi, Y., Tanaka, M., Tominaga, N., et al. 2017, PASJ, 69, 101
Valenti, S., Sand, D. J., Yang, S., et al. 2017, ApJL, 848, L24
Van Gorkom, K., Douglas, E. S., Ashcraft, J. N., et al. 2022, SPIE, 12180, 121805M
Van Gorkom, K., Douglas, E. S., Milani, K., et al. 2024, SPIE, 13092, 1309222
Van Gorkom, K., Anche, R. M., Mendillo, C. B., et al. 2025, JATIS, 11, 042203
Villar, V. A., Guillochon, J., Berger, E., et al. 2017, ApJL, 851, L21
Vincenzi, M., Brout, D., Armstrong, P., et al. 2024, ApJ, 975, 86
Wagner, K., Douglas, E., Ertel, S., et al. 2025, ApJL, 991, L44
Wagner, K., Follette, K. B., Close, L. M., et al. 2018, ApJL, 863, L8
Wakeford, H. R., Sing, D. K., Deming, D., et al. 2018, AJ, 155, 29
Waxman, E., & Katz, B. 2017, in Handbook of Supernovae, ed. A. W. Alsabti & P. Murdin (Springer), 967
Welbanks, L., Madhusudhan, N., Allard, N. F., et al. 2019, ApJL, 887, L20
Wevers, T., Maccarone, T. J., Palmese, A., et al. 2026, arXiv:2606.17136
Winn, J. N., & Fabrycky, D. C. 2015, ARA&A, 53, 409
Witt, E. M., Fleming, B. T., Green, J. C., et al. 2021, SPIE, 11444, 1144409
Wong, K. C., Suyu, S. H., Chen, G. C.-F., et al. 2020, MNRAS, 498, 1420
Ygouf, M., Pueyo, L., Soummer, R., et al. 2015, SPIE, 9605, 96050S–96050S–9
Zhou, Y., Bowler, B. P., Wagner, K. R., et al. 2021, AJ, 161, 244
Zhou, Y., Bowler, B. P., Yang, H., et al. 2023, AJ, 166, 220
Zhou, Y., Bowler, B. P., Sanghi, A., et al. 2025, ApJL, 980, L39
Zhou, Y., Sanghi, A., Bowler, B. P., et al. 2022, ApJL, 934, L13